Heating Phase of DST—

Boreholes 42 and 43: These boreholes extend from AOD toward the HD and were used for mine-by as discussed above. Observed and predicted deformations for these boreholes after heating started are shown in Figures 129 and 130. Figure 129 shows that for the first 250 days, the basecase model simulated deformation very well for Borehole 42. After 300 days, the observed deformation rate is higher than predicted, and the fit is not as good.

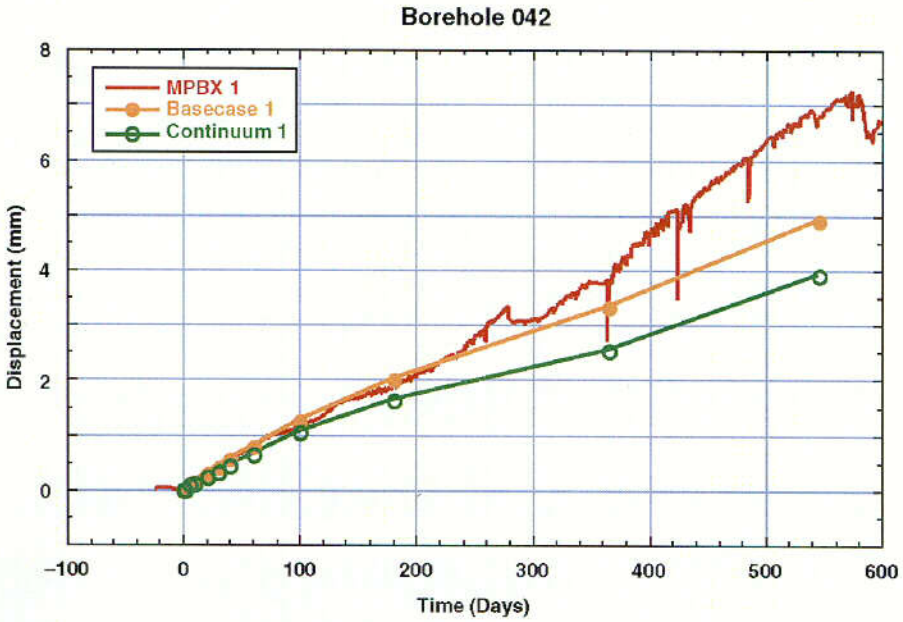

Figure 129. Observed and Predicted Deformation for BH 42.

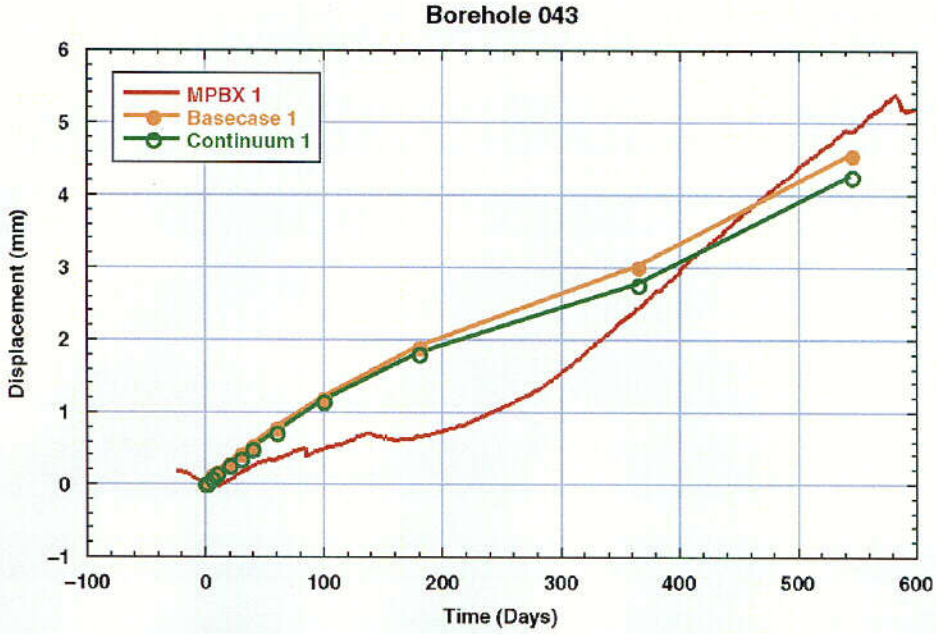

Figure 130. Observed and Predicted Deformation for BH 43.

C01

At 240 days the basecase model matches the prediction to better than 10%, but at 545 days the basecase model predicts 70% of the observed value. The continuum model underpredicts the deformation throughout the 545-day period and, at 545 days, the value predicted by the continuum model is 57% of the observed value.

Observed and predicted behavior for BH 43 is shown in Figure 130. This borehole is roughly parallel to BH 42 (see Figure 123) and, as expected, the predicted deformations are similar to those predicted for BH 42, with the basecase model predicting more deformation than the continuum model.

However, the observed deformation for BH 43 anchor 1 shows a much different trend than deformation observed for borehole 42, with a low rate of deformation for the first 200 days of heating. After 200 days, the deformation rate increases dramatically to slightly less than the 0.016 mm/day observed for BH 42 after approximately 300 days.

Boreholes 81 and 82: Figures 131 and 132 show results for boreholes 81 and 82. These boreholes are parallel to the HD, 3.4 m above the center of the wing heaters, and are collared in the connecting drift. These figures show that both the basecase and the continuum models substantially underpredict the observed deformation for Anchor 6 in each of these boreholes.

The data show very little movement for the first 20 days, followed by increasing deformation (expansion), with boreholes 81 and 82 showing 5 and 6 mm of expansion, respectively, by 545 days of heating. In contrast, the predictions show negative deformation (compression) for the first 80 days, followed by expansion, but the predicted rate of expansion is much slower than that observed.

The observations and model predictions follow the same general trend between 80 and 400 days, during which both observed and predicted displacements rise at a diminishing rate. After 400 days, the observed displacements rise at an increasing rate, a feature which is not matched by the model. The total predicted deformation of approximately 1 mm is a factor of 6 lower than the 6 mm observed.

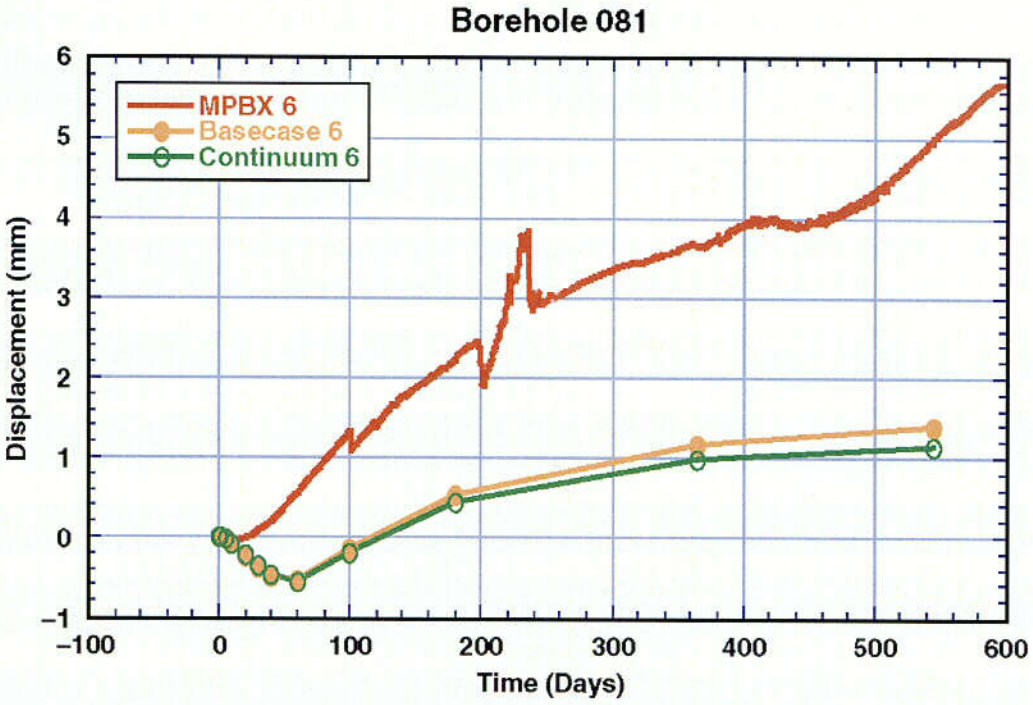

Figure 131. Observed and Predicted Deformation for BH 81.

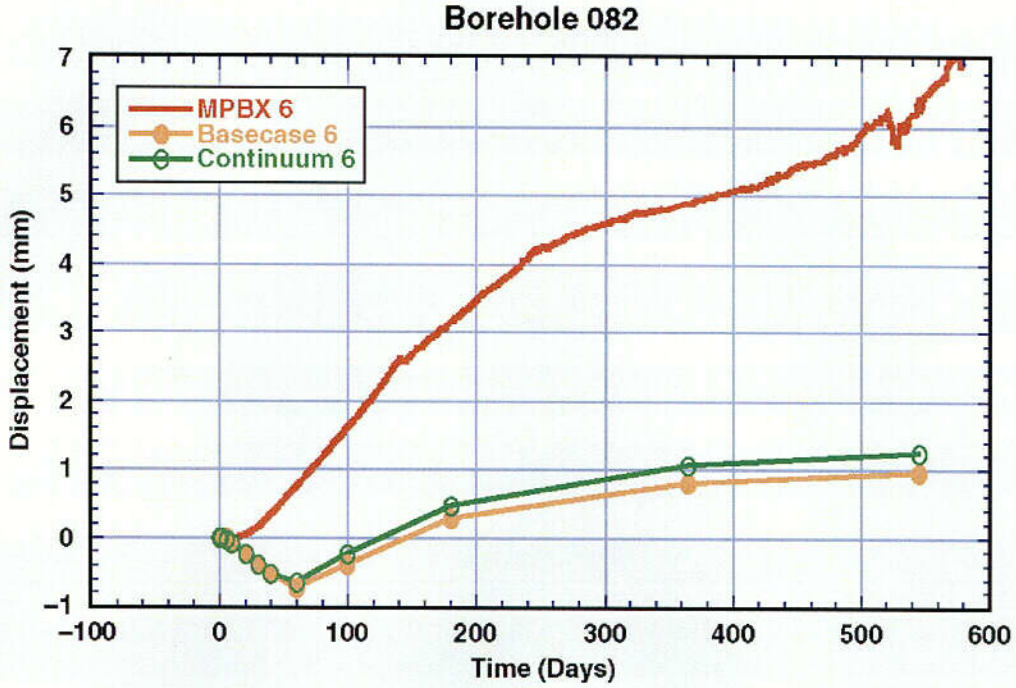

Figure 132. Observed and Predicted Deformation for BH 82.

C02

Boreholes 147, 148, and 149: These boreholes are located in the crown of the HD, approximately 13 m from the bulkhead, and form along with BH 150 the first fan of three MPBX boreholes in the HD. The observed and predicted deformations for boreholes 147, 148, and 149 Anchor 4 are shown in Figures 133, 134, and 135.

Results for BH 147 (Figure 133) show that observed deformation begins immediately upon start of heating, while the predicted deformation doesn't begin until 40–50 days after heating. After 50 days the predicted slope is very similar to observation, and overall magnitude at 545 days is 5 mm for prediction vs. approximately 5.5 mm for observation. Thus the predicted value is 90% of the observed value. The basecase model predicts larger magnitude of deformation and starts somewhat sooner than the continuum model. Note that the sharp drops in deformation are interpreted to be associated with temperature changes in the borehole and not actual rock movements.

Predicted and observed deformations for BH 148 are shown in Figure 134. This borehole is angled toward the AOD. This figure shows that the observed displacement increases much more quickly after the start of heating than does the predicted displacement, but the difference is not as great as observed in BH 147.

A change in slope occurs at approximately 20–30 days, after which the slope is linear until approximately 250 days, when the rate of displacement decreases somewhat. The simulated deformation shows a lag in initial response similar to that predicted for BH 147. After approximately 60 days the slope of the basecase model matches the observation very well, while the expansion rate for the continuum model is too high. At 400 days the basecase model matches the observed value almost exactly.

Predicted and observed deformations for BH 149 are shown in Figure 135. This figure shows that the basecase model predicts behavior very well. This borehole is vertical in the crown (see Figure 123).

In initial behavior, the rock deforms during the first 10 days, while the predicted deformation does not start until after day 20. Agreement with data at 545 days is excellent, within 5%. The basecase model fits somewhat better than the continuum model

Examination of the three boreholes (147, 148, 149) as a group shows that deformation for BH 147 is greater than for BH 148 and 149. That is, at 400 days, boreholes 147, 148, and 149 show 4.4, 3.4, and 3.6 mm of displacement, respectively. This indicates that rock on the side away from the AOD is deforming more than the rock between the HD and the AOD. The basecase model predicts 3.6, 3.4, and 3.4 mm, respectively, while the continuum model predicts 3.4, 3.8, and 3.8 mm, respectively, for these boreholes at 400 days. Thus, the basecase model correctly predicts the trend of the measurement, as it indicates larger deformation for BH 147, and equal deformation for boreholes 148 and 149. The continuum model does not capture this behavior as well.

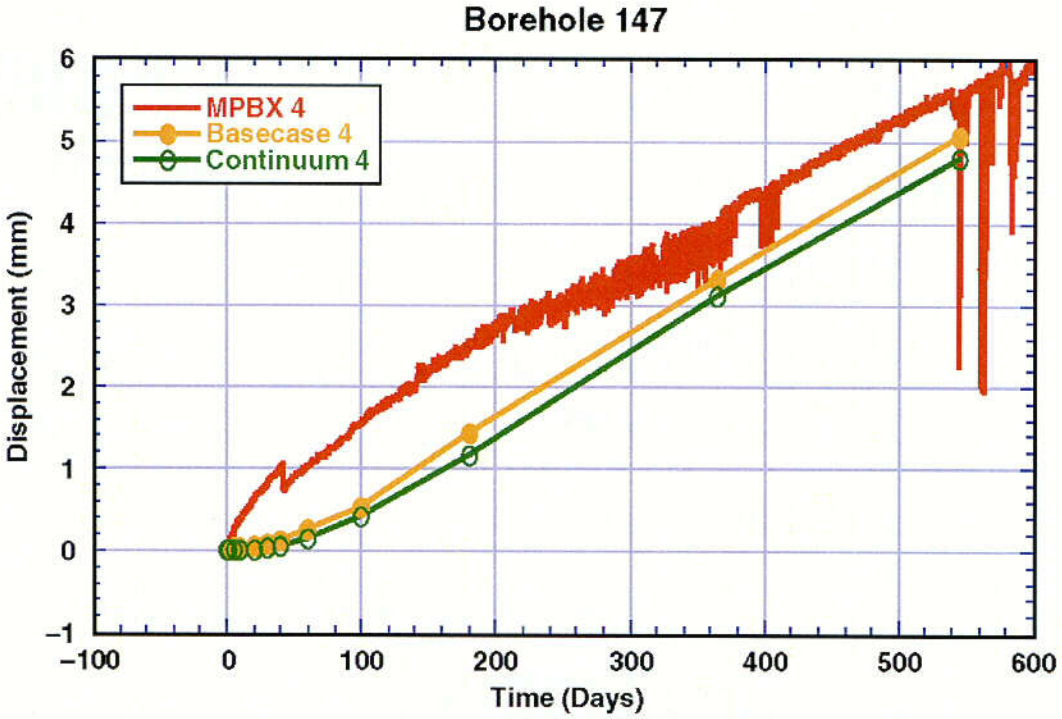

Figure 133. Observed and Predicted Deformation for BH 147.

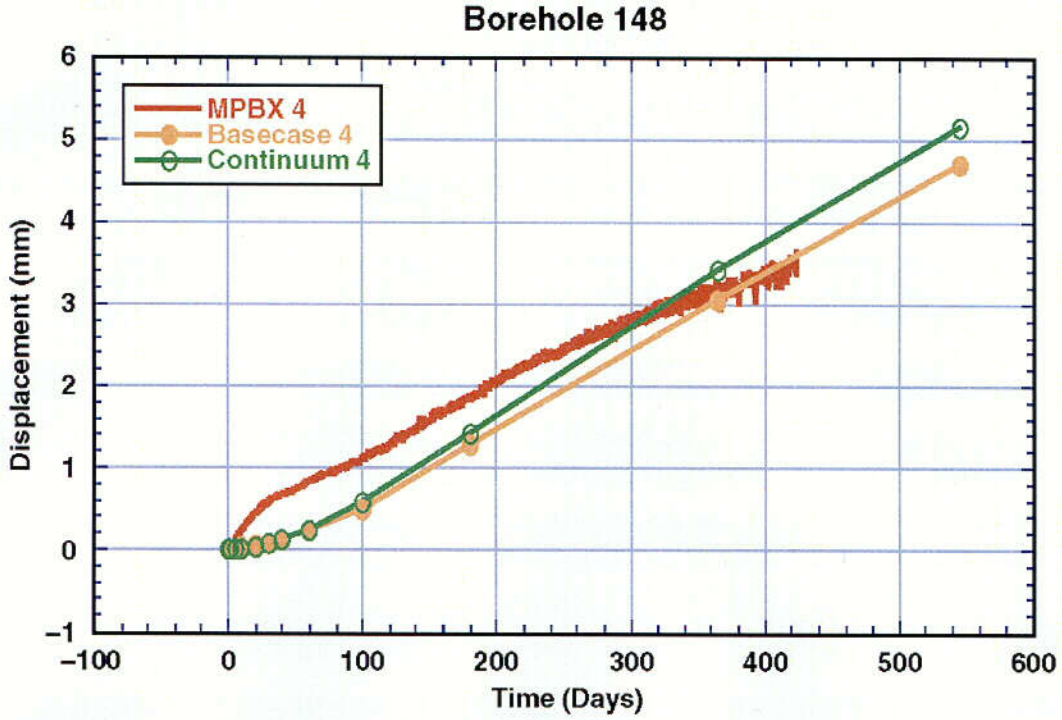

Figure 134. Observed and Predicted Deformation for BH 148.

C03

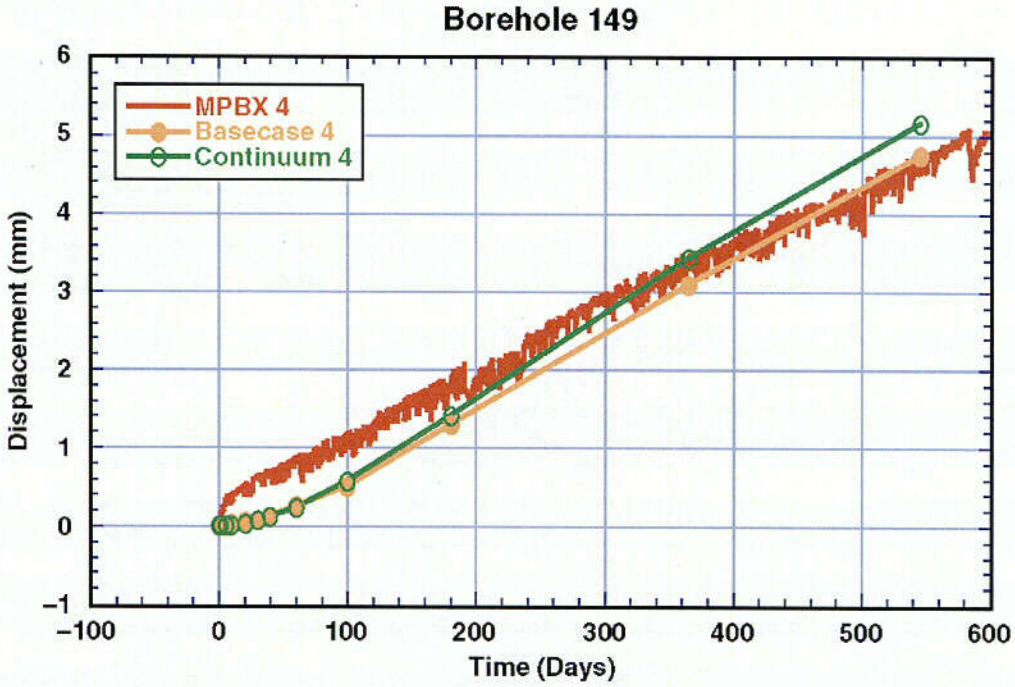

Figure 135. Observed and Predicted Deformation for BH 149.

Borehole 150: Results for BH 150 are shown in Figure 136. This is a vertical down borehole in the floor of the drift, and is in the same cross-section as boreholes 147, 148, and 149. Again, the predicted deformation lags the observations during the first 20 days of heating, after which the slopes are similar.

The basecase model is closer in magnitude to the observed deformation at MPBX 4 by about 0.3 mm (day 545) than the continuum model, and the deformation rate appears to be slowing in the data. This change in rate is not predicted by the model. The magnitude of the prediction at day 545 is well within 10% of the observed value (4.8 mm predicted by the basecase model vs. 5.0 mm observed).

Borehole 156: This is a vertical up borehole located in the middle fan of the MPBX boreholes shown in Figure 123. Observed and predicted deformations are shown in Figure 137. For this borehole, predictions show a small negative deformation for the first 100 days, while observations during this time show a rapid expansion. After 100 days the slope of the predicted deformation is very similar to that of the observed. At 545 days the estimate of 3.5 mm is within 20% of the 4.7 mm observed value.

Borehole 180: This is another vertical up-hole in the crown. Results of observations and predictions (Figure 138) are similar to those for boreholes 149 and 156. That is, the model shows low or negative expansion for the first 100 days and lags the observed deformation. The slope of the model and the observations after 100 days are very similar through 330 days. Observed deformation data are unavailable between 330 and 540 days. Data are available after 540 days, and the predicted value of 3.5 mm is within 10% of the observed value of 3.7 mm at 545 days. Continuum and basecase model predictions are very similar, as there are few fractures currently mapped in this region.

C04

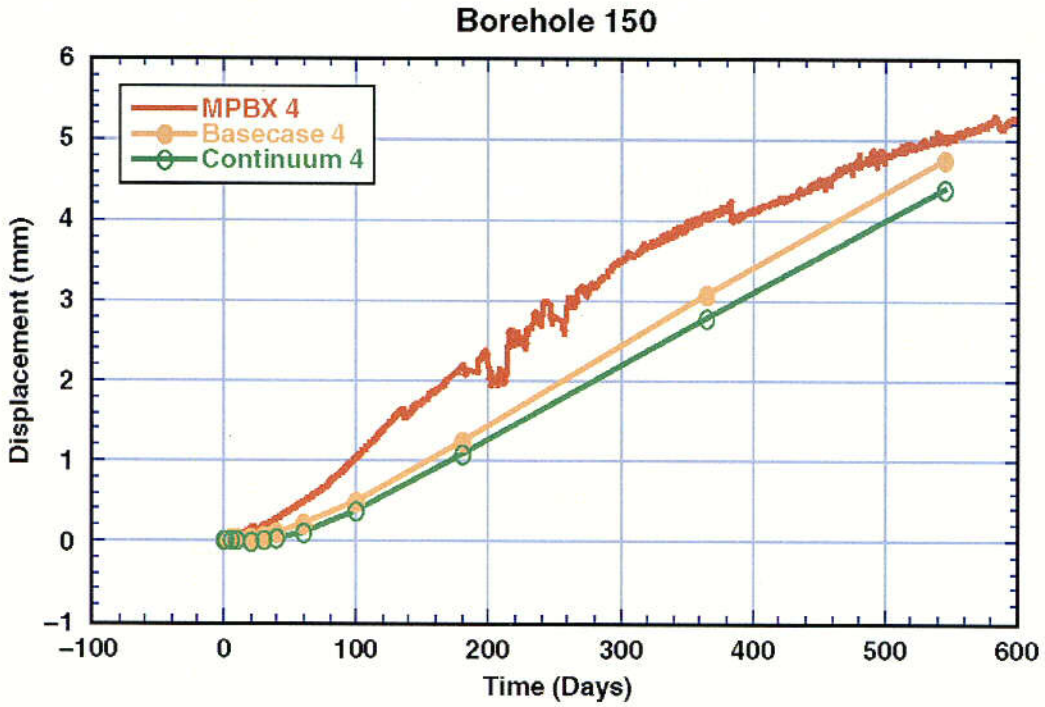

Figure 136. Observed and Predicted Deformation for BH 150.

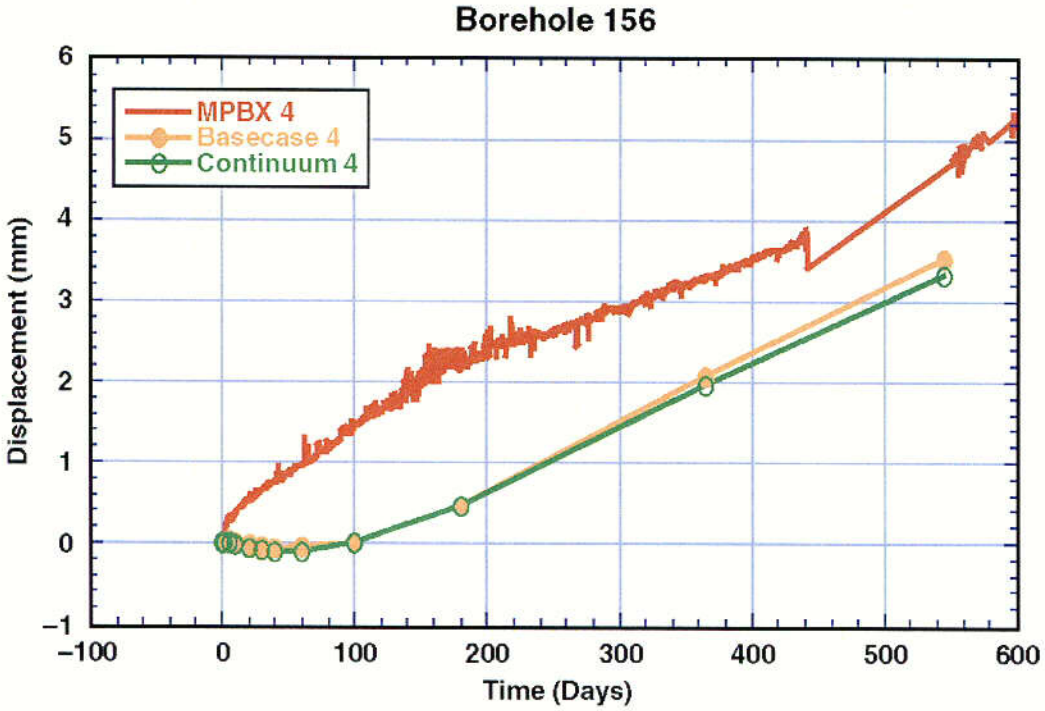

Figure 137. Observed and Predicted Deformation for BH 156.

C05

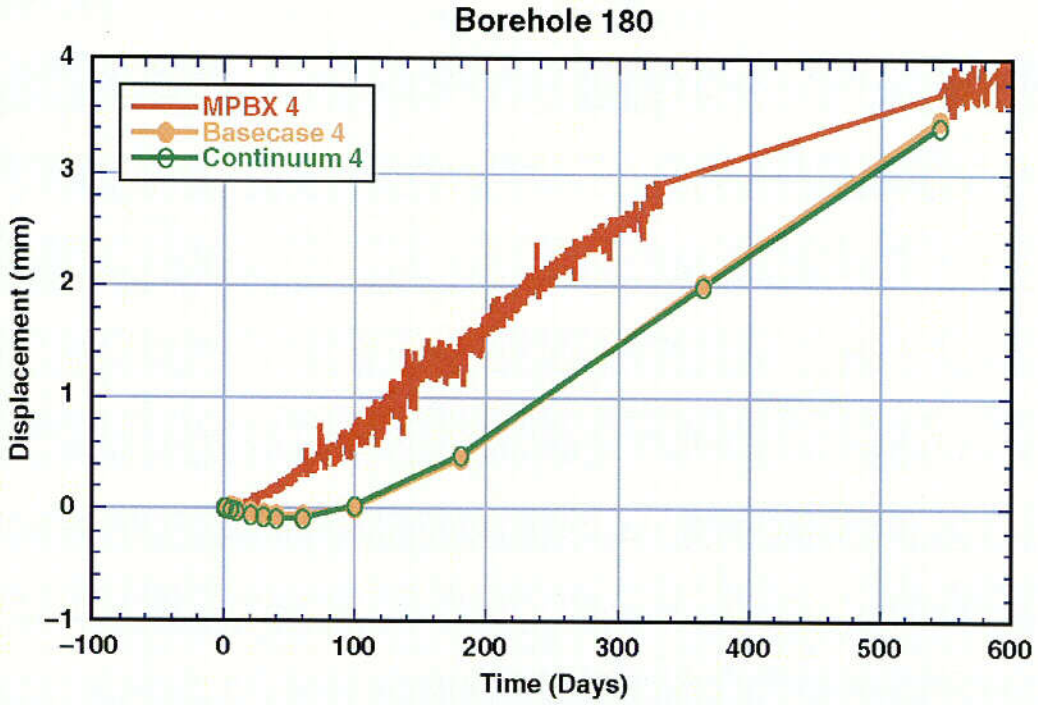

Figure 138. Observed and Predicted Deformation for BH 180.

Statistical Validation of THM Model. In addition to the qualitative comparison of predicted and observed deformation for the DST, three statistical measures were used to compare measured and simulated displacements. These measures are the root-mean-square difference (RMSD), the mean difference (MD), and the normalized-absolute-mean difference (NAMD). The application of these statistical measures provides a quantitative approach that complements the qualitative comparison of the predicted and measured deformations. These statistical measures are based on standard statistics (Bowker and Lieberman 1972) which have been modified to better adapt to interpretation of measured and simulated behavior in the thermal test.

The root-mean-square difference (RMSD) for a specific time after the start of heating is defined as:

$$RMSD = \left[\frac{\sum_{i=1}^{N} \left(d_{sim,i} - d_{meas,i} \right)^2}{N} \right]^{1/2}$$

where $d_{sim,i}$ and $d_{meas,i}$ are the simulated and measured displacements for the ith MPBX anchors. N is the number of anchors compared at a particular time. The anchors used in this analysis are listed in Table 8. The smaller the RMSD the better the agreement between simulated and measured displacements.

C06

The mean difference (MD) for a specific time is defined as:

$$MD = \frac{\sum_{i=1}^{N} \left[d_{sim,\,i} - d_{meas,\,i} \right]}{N}$$

A positive MD indicates an overestimate or overprediction of displacements, whereas the converse applies for a negative MD.

The normalized absolute mean difference (NAMD) for a specific time is computed using:

$$NAMD = \sum_{i=1}^{N} \left| \frac{d_{sim,\,i} - d_{meas,\,i}}{d_{meas,\,i}} \right| * \frac{1}{N}$$

The NAMD provides a percentage of the absolute difference between measured and simulated displacement relative to the measured displacement.

Figure 139 shows the time history for each of the three statistical measures (RMSD, MD, and NAMD) used to assess the agreement between measured and calculated displacements for both the base case (discrete model) and the sensitivity case (continuum model).

The overall agreement is reasonable for this initial analysis of the mechanical behavior in the DST. Also, it appears that the two cases considered (discrete and continuum models) do not differ substantially in their ability to simulate the measured displacements. These findings will need to be updated in future statistical analyses that will involve a more robust comparative analysis by including substantially more MPBX anchors. The RMSD shown in Figure 139 shows a general linear increase after the initial 20 days of heating for both cases considered. The 500-day magnitudes are slightly less than 3 mm. Figure 139 shows that the MDs for both cases are also quite similar for the times considered. These MDs, which are averages of all MDs determined at a specific time, range from 0.0 mm to –0.5 mm over the initial 500 days of heating. Upon further examination of the MDs for individual anchor locations, the MD ranges from –4.5 mm to 2.5 mm. Consequently, the MDs in this analysis tend to offset each other, resulting in the trends shown in Figure 139. The NAMDs shown in the figure are as high as 250 percent during the initial 100 days of heating. Thereafter, they are better but still average approximately 150 percent over the next 400 days. Upon examination of individual MPBX boreholes/anchors, it becomes apparent that a few of the MPBX boreholes contribute to the substantially large NAMDs. In some instances, these large NAMDs reflect comparatively small measured displacements. This behavior is noticeably present in the long longitudinal MPBX boreholes (81 and 82) that are slightly above and outside the Heated Drift. This general and unfavorable trend suggests that modeling of the displacements parallel to the axis of the Heated Drift will need to be reevaluated including characterization of fractures or discontinuities.

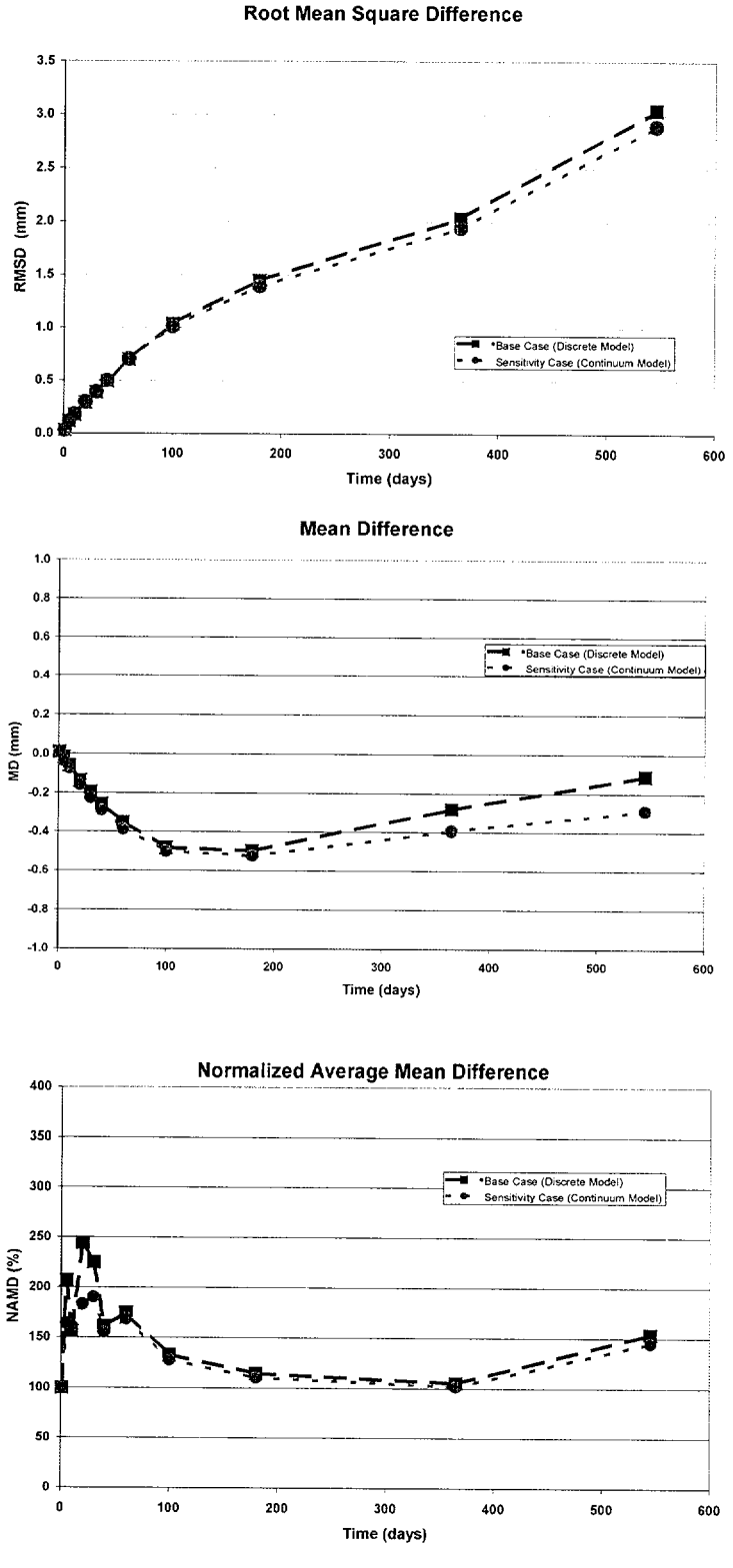

Figure 139. Statistical Measures for Comparative Analyses of Drift Scale Test Displacements.

5.3.2 Large Block Test

Test Description and Model Development

The Large Block Test (LBT) was conducted at Fran Ridge, near Yucca Mountain, Nevada, and comprised one phase of the field-scale thermal testing program of the Yucca Mountain Site Characterization Project. The particular objective of the LBT was to monitor and characterize coupled THMC processes in an isolated block of fractured rock subject to a one-dimensional thermal gradient (Wilder et al. 1997). Because the block is an unconfined and well-mapped fractured rock mass, it is a good candidate for analysis using discontinuum models.

The LBT was conducted on a rectangular prism of rock 3 m × 3 m in cross-section and 4.5 m high that was exposed from an outcrop by excavating the surrounding rock. Detailed geologic mapping showed that two subvertical sets of fractures and one set of subhorizontal fractures intersect the block. The subvertical fracture sets are approximately orthogonal, with spacings of 0.25 to 1 m and are oriented generally in the NE–SW and NW–SE directions. Moreover, a major sub-horizontal fracture is located approximately 0.5 m below the top surface.

To create a one-dimensional thermal field within the block, heaters were placed in the rock to simulate a plane heat source at a height of 1.75 m from the base of the block, and a steel plate fitted with heating/cooling coils was mounted on the top of the block. This plate was connected to a heat exchanger to allow thermal control of the top surface. The block was heated for more than 12 months, from Feb. 27, 1997, until March 10, 1998.
The overall three-dimensional mechanical response of the rock to the heating was monitored using six multiple-point borehole extensometers (MPBXs). Three were oriented horizontally in the N–S direction; two were oriented horizontally in the E–W direction, and one was oriented vertically. The geometry of the heaters, MPBX boreholes, and one temperature borehole is shown in Figure 140.

A THM model for the LBT has been formulated using the general approach presented above. This model incorporated the general geometry of the LBT. Data for the simulations is given in Tables 4, 6, and 7. The input and output files for the Large Block Test model validation simulations have been submitted to the TDMS (DTN: LL010703623123.01).

Temperatures. Deformation of the LBT was calculated at times of 0, 10, 25, 55, 85, 115, 145, 182, 200, 275, 340, 350, 375, 385, 395, 410, 430, and 450 days after the start of heating. The temperatures in this analysis were derived from the TH analysis reported in CRWMS 2000, Section 6. Files containing Cartesian coordinates and temperatures for the model region simulated by NUFT were obtained at each time. The NUFT model assumes symmetry in the block; consequently these files contained values for one quadrant of the region simulated in 3DEC. The 3DEC calculations include the entire volume of the block, as the fractures are not symmetric. A 3-dimensional temperature field for 3DEC was produced from the NUFT temperatures by reflecting the temperatures about the appropriate vertical planes. This was done as follows. Temperatures from the NUFT model and their coordinates were input into EarthVision along with an array of

grid points generated by 3DEC for the LBT model domain at each calculation time. EarthVision performed a three-dimensional interpolation of the 3D NUFT model temperatures to provide an interpolated temperature for each calculation time at each of the 3DEC model grid points. The grid point temperatures were then input into 3DEC as a separate input file for each calculation time.

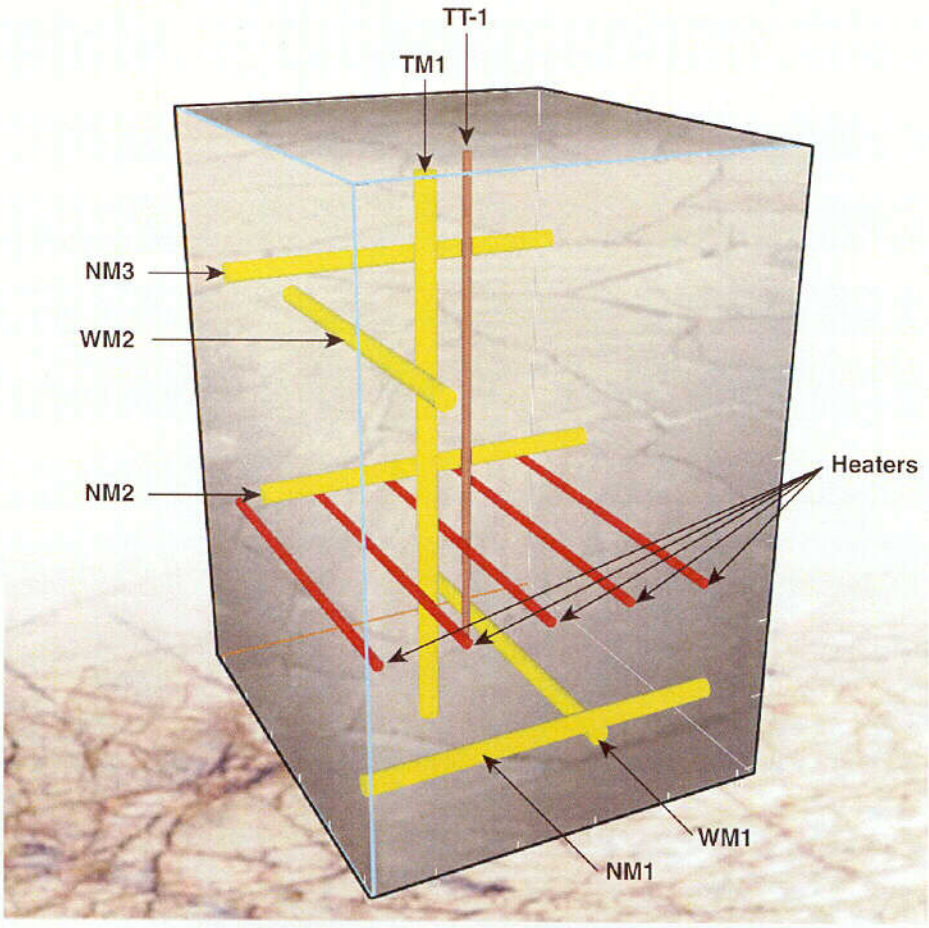

Figure 140. MPBX Borehole Locations in the Large Block Test.

Fractures. Fractures used in the simulations were taken from the LBT fracture data set described in Wilder et al. (1997, Section 2.2). Particular fractures used in the simulations are discussed below. The fractures were assumed to have no tensile strength.

Model Geometry. The spatial domain for the LBT model is shown in Figure 141, top left. This model domain extends 23 m beneath the ground surface and 23 m out from each vertical face of the LBT, so that the fixed displacement boundary conditions can be applied far from the heated portion of the block. At these distances thermal expansion cannot reasonably be expected, so that fixed displacement boundary conditions may be applied with confidence.

C07

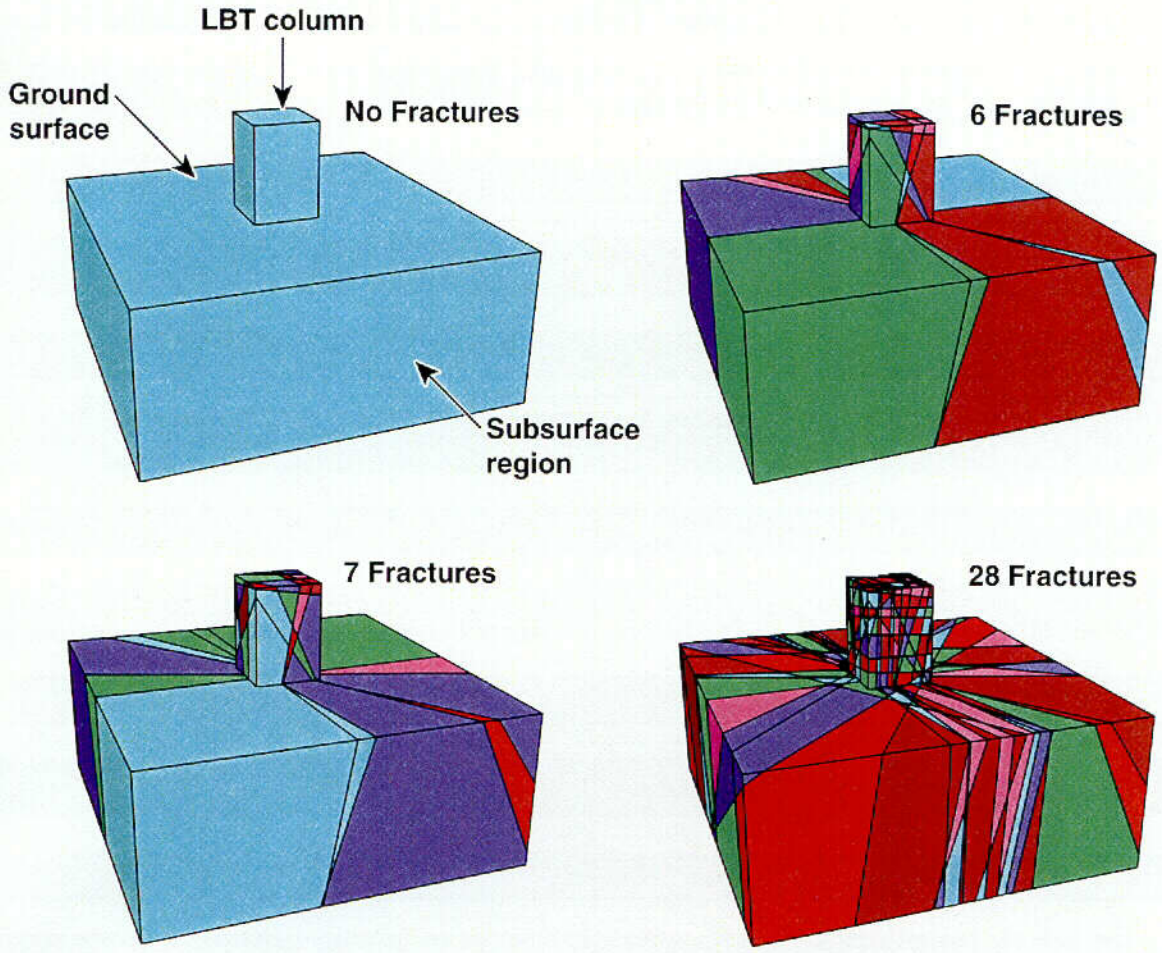

Figure 141. Spatial Domain for the Model.

Boundary Conditions. Roller boundary conditions were imposed on the four vertical sides and on the base of the subsurface region. These boundary conditions impose a zero displacement restriction on normal displacements along these surfaces, but allow parallel (in plane) displacements. Thus, horizontal displacements are permitted along the base of the block and vertical displacements are permitted along the sides of the subsurface region. Fixed displacement boundary conditions provide an upper bound on thermal stresses because outward displacements of the model sides, which would relieve built-up stresses, are not allowed.

The base of the block was fixed in the vertical direction to prevent the rock at 23 m below the LBT from moving vertically. The top of the block is allowed to move vertically. This is appropriate because the LBT column is unconfined, whereas the base of the model is supported by the underlying rock. A fixed stress boundary condition, equal to atmospheric pressure, is applied to the top and sides of the LBT columnar region and to the ground surface region in the model.

C08

Rock Properties. Input parameters for the LBT simulation are provided in Table 6. Calculated or assumed parameters are listed in Table 7.

Simulations. A series of simulations (referred to as "Models" in the following discussion) were conducted to evaluate the effect of number of fractures and of Coefficient of Thermal Expansion (CTE) on the mechanical behavior. The simulations are listed in Table 10 and the fracture geometries of the model domain for the various simulations are shown in Figure 141.

Table 10. Summary of THM Simulations of the LBT

Model #	Number of Fractures	CTE ($\times 10^{-6}$/°C)	Comment
1	0	5.27	Continuum model
2	6	9.73	High CTE with 6 major fractures
3	6	5.27	Low CTE with 6 major fractures
4	7	5.27	Same as 3 with one additional fracture
5	28	5.27	All fractures included in fracture analysis

Results for Large Block Test

The 3DEC model was configured to produce displacement values at the locations of the MPBX anchors discussed above. Deformation in the vertical direction was monitored in borehole TM1, and predicted displacement is compared with observed displacement for anchor TM1-4 in Figure 142a for the first 100 days of heating. This figure plots results for each simulation along with the observed displacement and shows that while Model 2 with high CTE matches the early thermal deformation up to 20 days, it overpredicts the deformation at 100 days by more that a factor of 2. Predictions produced by the other four models, with lower CTE, are quite acceptable as they underpredict the magnitude of the displacement by only a few tenths of a millimeter. The continuum and fractured models produce similar estimates, and the response of all of these models lags the observed deformation during the first 40 days. Thus, the number of fractures had very little effect on predicted deformation for the vertical direction.

Predicted deformation during cooldown is compared with field measurement at anchor TM1-4 in Figure 142b. This plot shows that the continuum model (Model 1) fits both the shape and magnitude of the observations, while Model 3 with six fractures also approximates the observations quite well.

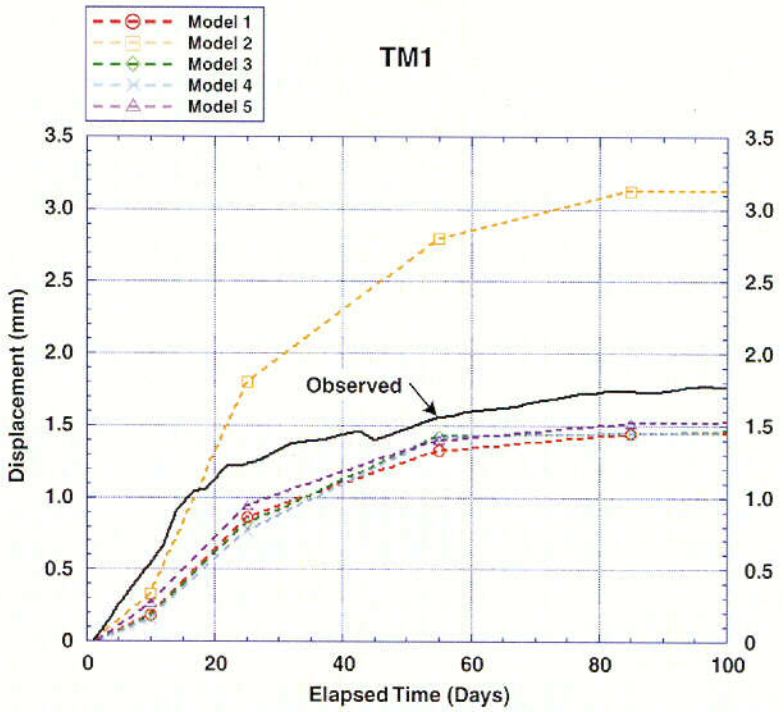

Figure 142a. Simulated Deformation in the Vertical Direction Compared with Field Measurements for Anchor TM1-4.

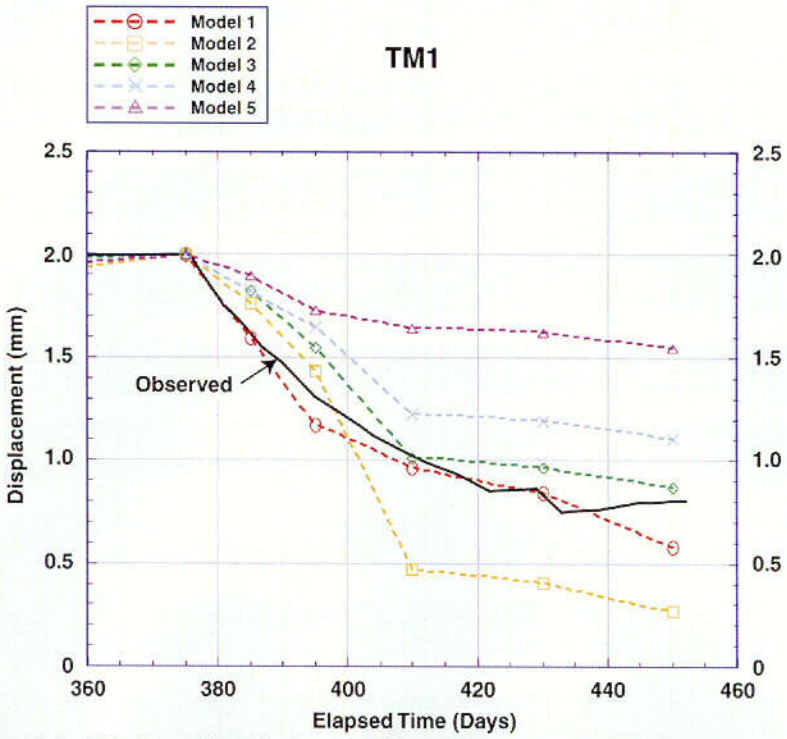

Figure 142b. Simulated Deformation during Cooldown Compared with Field Measurement at Anchor TM1-4.

C09

MPBX boreholes NM1 and WM1 were located close to the bottom of the block and in orthogonal directions. Measured and predicted displacement values for anchor NM1-4 are plotted in Figure 143a. This figure shows that at this location, Model 3 provides the best match to the observations. Model 2 overpredicts displacement by nearly a factor of 2, while the continuum model (Model 1) underpredicts the deformation. Models 1, 3, 4, and 5 bracket the observed values, with Model 1 underpredicting for the first 100 days and Models 4 and 5 overpredicting at 100 days. This plot indicates that while Model 3 (6 fractures) slightly underpredicts deformation, adding one fracture (Model 4) caused more displacement at this location, but adding many fractures (Model 5) caused underprediction during the first 25 days and overprediction after 25 days.

Results for NM1-4 during cooldown are shown in Figure 143b. This figure shows that at this location Model 3 matches the magnitude of the displacement, but does not accurately predict the cooling path. Model 2 overpredicts the displacement and best approximates the slope of the curve during the first 20 days of cooling. Models 1, 4, and 5 underpredict the amount of recovery during cooldown. The least contraction is predicted by Model 5, the highly fractured rockmass.

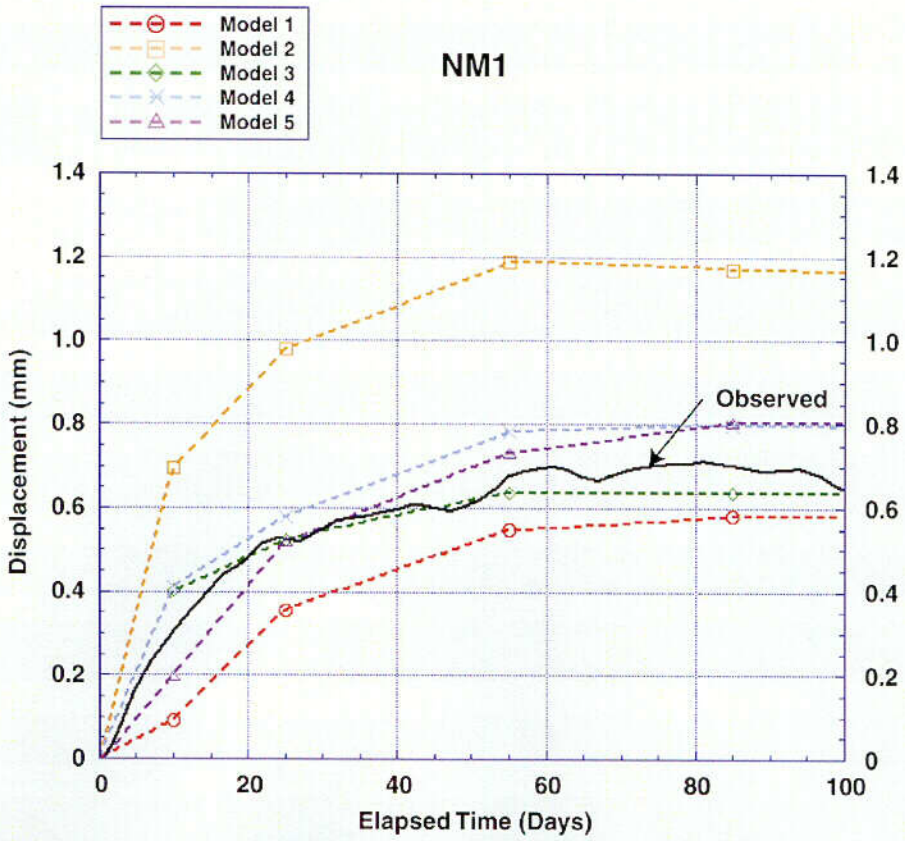

Figure 143a. Measured and Predicted Displacement Values for Anchor NM1-4.

C10

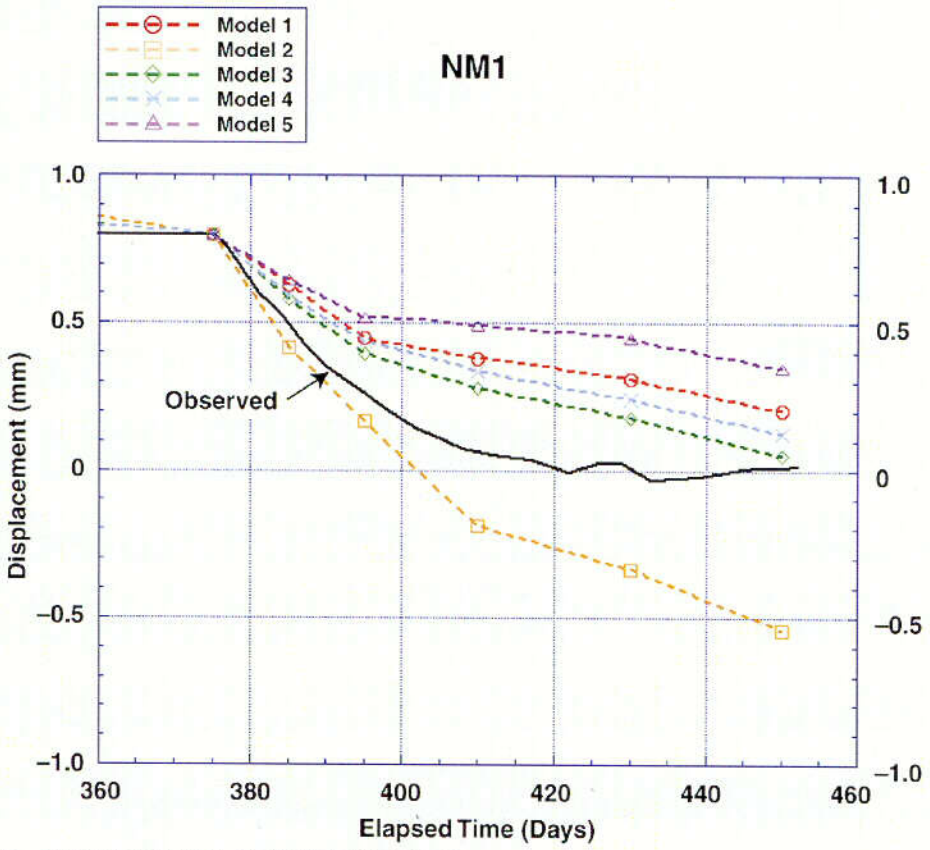

Figure143b. Results for NM1-4 During Cooldown.

Data and predictions for the first 100 days of heating for WM1 are shown in Figure 144a. This plot shows similar results to Figure 143a in that Model 2 overpredicts by nearly a factor of two, and models 1, 3, 4, and 5 bracket the behavior. The highly fractured model (Model 5) best approximates the response during the first 20 days; Models 3 and 4 overpredict the displacement during the first 10 days, but are within about 0.05 mm of the observed displacement at 100 days. Model 1 underpredicts the displacement by between 0.1 and 0.15 mm throughout this time interval.

Modeling results for WM1 during the cooldown period are shown in Figure 144b. These results are similar to the results for NM1 in that the continuum model (Model 1) most closely approximates the observed cooldown. The high CTE model (Model 2) overpredicts the deformation, while the other models underpredict the displacement. Interestingly, these results show that adding fractures to the model causes less recovery during cooldown. This may be because fracture slip is essentially unrecoverable under unconfined stress conditions.

C11

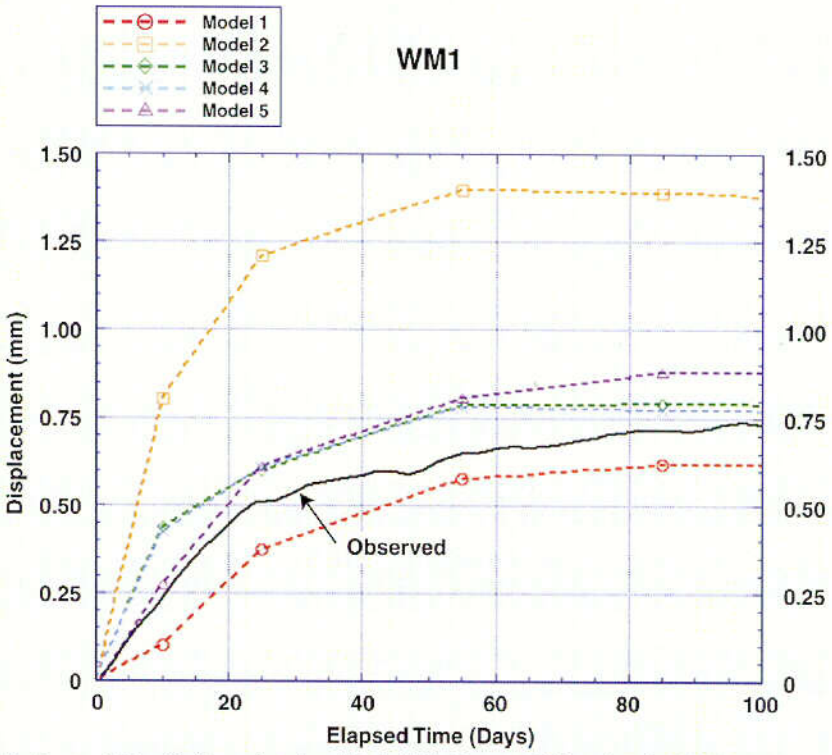

Figure 144a. Data and Predictions for the First 100 Days of Heating for WM1.

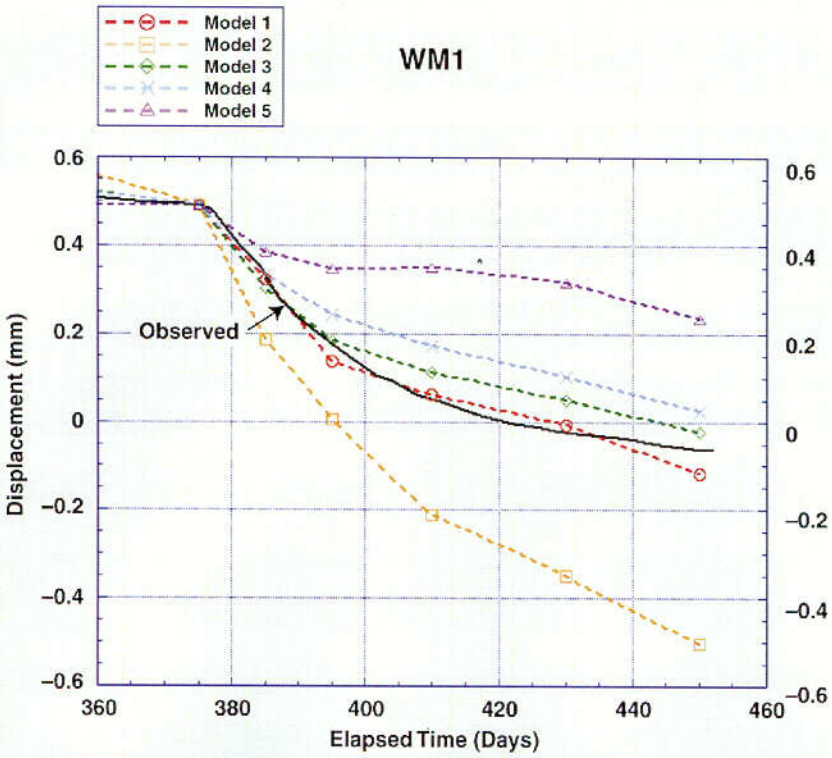

Figure 144b. Modeling Results for WM1 During the Cooldown Period.

C12

Figure 145 presents simulated and observed displacements for borehole NM2, which was located near the heater plane. This figure shows that the continuum model (Model 1) underpredicts the displacement for anchor NM2-4, while the high CTE model (Model 2) predicts the deformation relatively well during the first 10 days, but overpredicts the magnitude of the total deformation at 40 days by nearly a factor of 2. Models 3, 4, and 5 produce similar results, and both Models 4 and 5 cross over the observed deformation at 40 days. Of these three models, Model 5 provides the best fit to the data for the first 40 days, indicating that rock in this region is highly fractured.

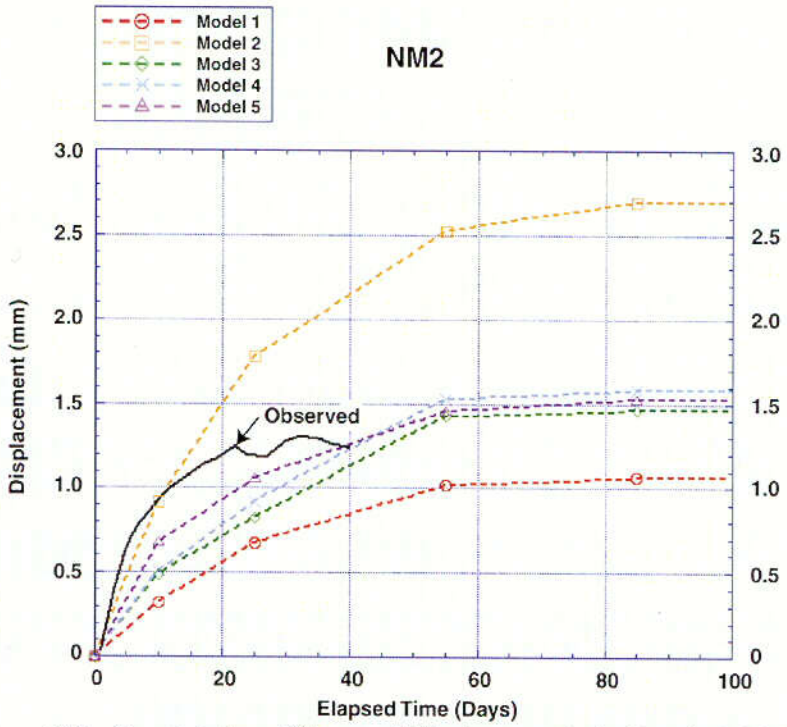

Figure 145. Simulated and Observed Displacements for Borehole NM2.

The MPBX instrumentation in borehole WM2 functioned throughout the test and data for anchor WM2-4 for the entire test is shown along with simulated displacements in Figure 146. This figure shows that for this anchor, Models 3 and 4 did a good job of predicting the deformation over much of the test duration. Model 3 predicts slightly less displacement than Model 4, and from 50 to 100 days Model 4 is closer to the observations, while from 120 to 220 days Model 3 fits slightly better. Models 3 and 4 also capture the cooldown relatively well. They underpredict the total amount of cooldown displacement, by 0.4 mm, and also show some contraction of the block about 270 days that is not reflected by the observation. Models 1 and 5 both underpredict maximum deformation by significant amounts (1.6 and 1 mm respectively). Model 2 overpredicts the maximum deformation, but does show the best fit to displacement during the first 20 days of heating. Model 5 does not show contraction with cooldown and Model 1 underpredicts the magnitude of the cooldown displacement. Model 2 correctly predicts the relative change in displacement during cooldown (1.8 mm) but the final value of 2.6 mm displacement is too high.

C13

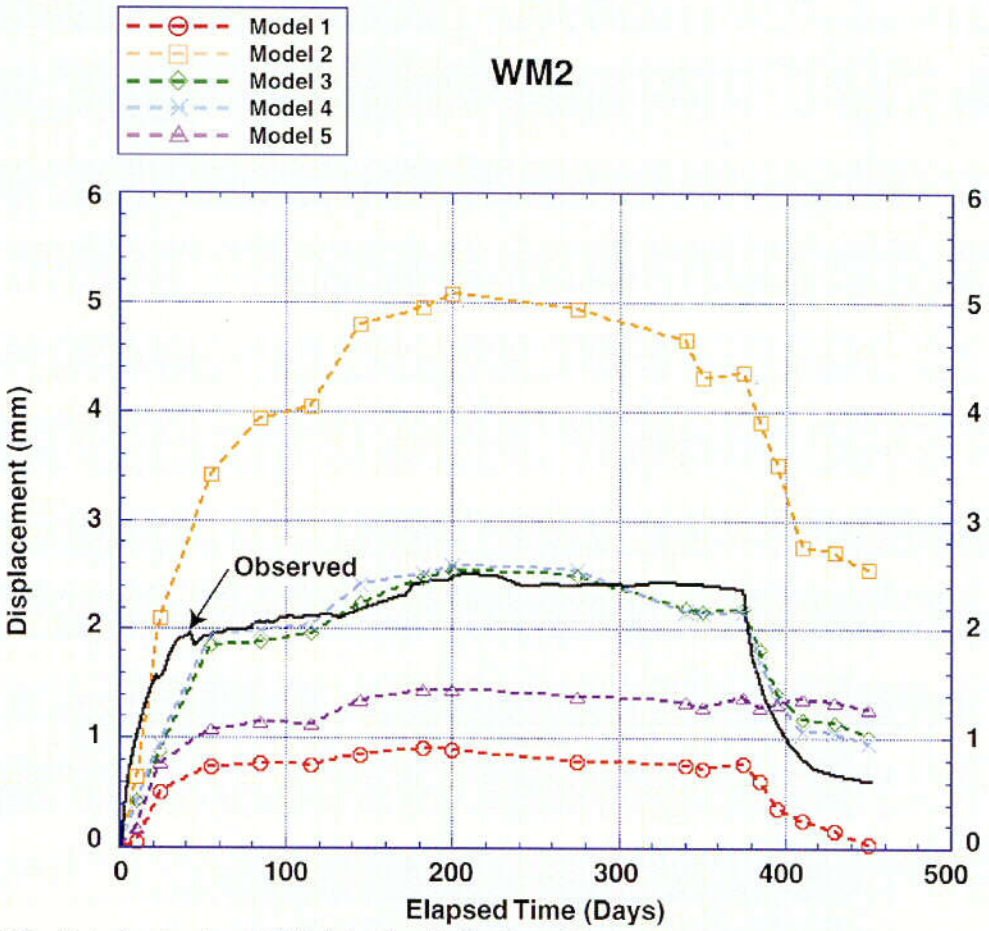

Figure 146. Data for Anchor WM2-4 for the Entire Test Shown Along with Simulated Displacements.

Continuous data are also available for anchor 4 of borehole NM3, the uppermost horizontal MPBX borehole in the block, and these data are shown with the model predictions in Figure 147. While the measured NM3-4 displacements are similar to those for WM2-4, with a maximum displacement between 2.5 and 3 mm, all of the models underpredict the measured NM3-4 displacements. This result differs considerably from that of the other MPBX boreholes. Adding one fracture to Model 3 to create Model 4 did increase the predicted NM3-4 displacements, but the increase was only a small fraction of that needed to compare well with the observations.

C14

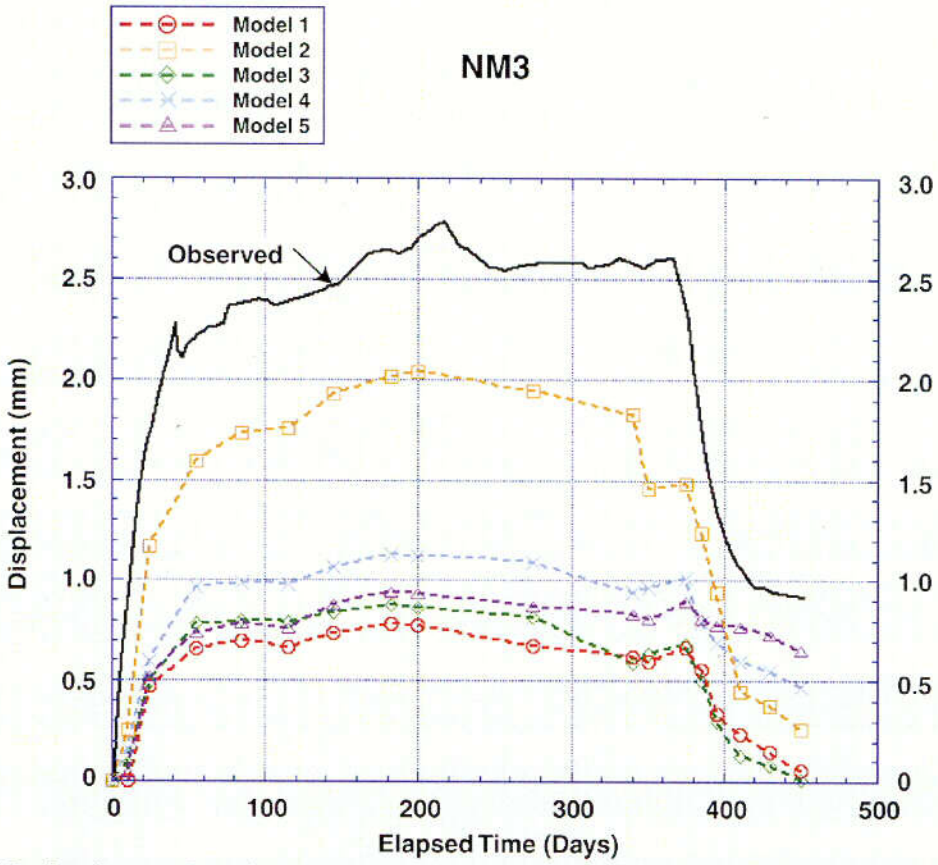

Figure 147. Continuous Data for Borehole NM3, Anchor NM3-4, Shown with the Model Predictions.

The results discussed above indicate that Models 3 and 4 provide the best overall fit to the observations. Model 1 fits the results at the bottom of the block relatively well.

The difference between the measured and predicted deformation during the first 50 days of heating is of interest as it relates to the transient response of the rock to the temperature field. Figures 143a and 144a show that for horizontal boreholes near the base of the block, deformation in Models 3 and 4 lead the observed displacements during the first 20 days. Figures 145 and 146 show that the observed deformation leads the predictions during the first 40 to 60 days of heating. Predicted and observed results for anchor WM2-4 for the first 100 days of heating are replotted in Figure 148 along with temperature data for the plane of the heater and the plane of WM2, respectively. This figure shows that during the first 30 days the observed deformation (WM2-4) can be correlated with temperature at the heaters (TT1-14), while the predicted deformation is correlated with temperature at the borehole location (TT1-22). This indicates that movement of the rock above the heater may be due to a far-field effect, and may imply that movement along fractures serves to propagate deformation.

C15

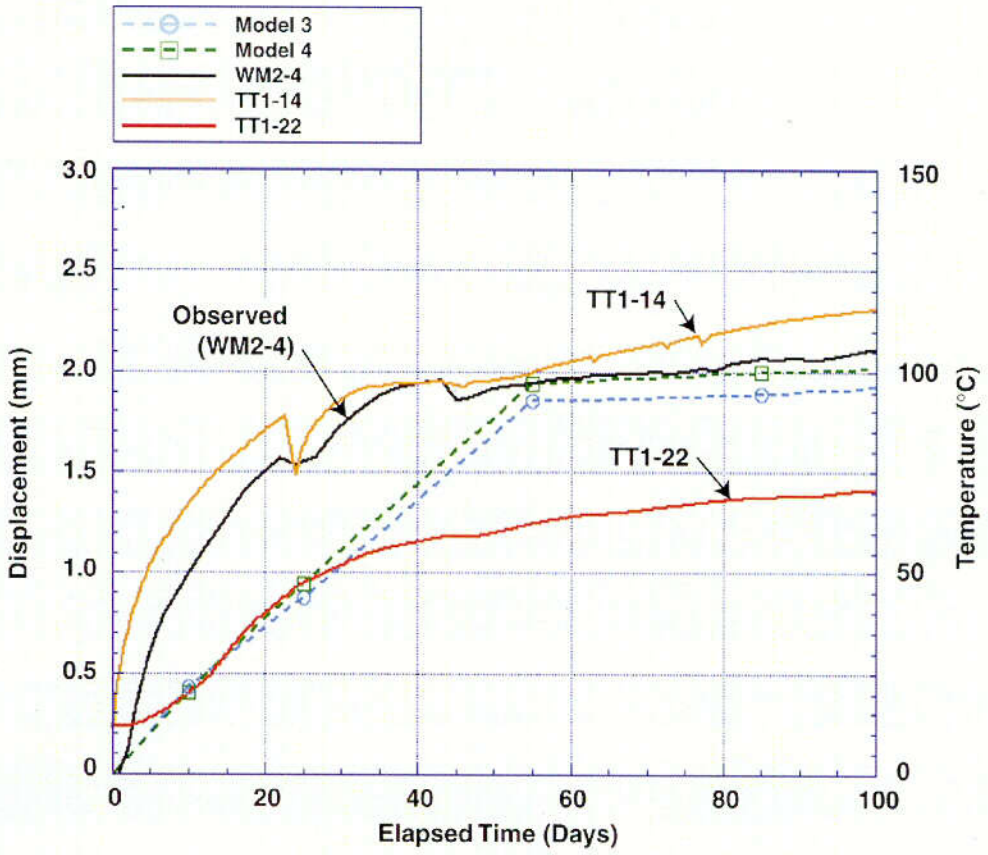

Figure 148. Predicted (Model 3, Model 4) and Observed (WM2-4) Displacements for Anchor WM2-4 during the First 100 days of Heating along with Temperatures for the Heater (TT1-14) and WM2 (TT1-22) Planes.

5.3.3 Conclusions

A coupled THM model has been formulated for analysis of TM behavior in fractured rock at Yucca Mountain. This model uses temperature computed by the NUFT TH code as input to the 3DEC distinct element mechanical code. The model has been used to simulate both the DST and the LBT. Predictions of deformation for these two tests have been made using the model in both a continuum mode and in formulations containing discrete fractures. Comparison of the predicted deformation with observations made using MPBX instrumentation shows that generally the predictions capture both the trend and the magnitude of the observations. Moreover, for both the DST and the LBT, the simulations containing discrete fractures more accurately predict the deformation behavior than do simulations with no fractures. This work indicates that not all fractures are active in the tests, and for the LBT, the deformation was controlled by a subset of 6-10 major fractures.

Results show that a CTE value of 5.27e-6/°C is appropriate for the LBT. This is consistent with the value determined for the Single Heater Test. However, a higher value of 9.73e-6/°C provided a good fit to deformation in the DST.

C16

The transient response of the predicted deformation at early times lags the observed deformation in both tests. This is caused in part by the lag in predicted temperatures when compared to observed temperatures. The TH thermal models must be improved in early times in order to correctly predict the TM behavior.

5.3.4 References

Bowker, A.H. and Lieberman, G.J. 1972. *Engineering Statistics.* 2nd Edition. Engelwood Cliffs, New Jersey: Prentice-Hall, Inc. TIC: 240460.

CRWMS M&O 1997. *Drift Scale Test Design and Forecast Results.* BAB000000-01717-4600-00007 REV 01. Las Vegas, Nevada: CRWMS M&O. ACC: MOL.19980710.0155.

CRWMS M&O 1998. *Drift Scale Test As-Built Report.* BAB000000-01717-5700-00003 REV 01. Las Vegas, Nevada: CRWMS M&O. ACC: MOL19990107.0223.

CRWMS M&O 2000. *Thermal Tests Thermal-Hydrological Analysis/Model Report.* ANL-NBS-TH-000001 REV 00. Las Vegas, Nevada: CRWMS M&O. ACC: MOL.20000505.0231.

CRWMS M&O 2001. *Coupled Thermal-Hydrologic-Mechanical Effects on Permeability Analysis and Models Report.* ANL-NBS-HS-000037 REV 00. Las Vegas, Nevada: CRWMS M&O.

Itasca Consulting Group, Inc. 1998. *3DECV2.0.* V2.0. STN:10025-2.0-00.

Jaeger, J.C. and Cook, N.G.W. 1979. *Fundamentals of Rock Mechanics.* 3rd Edition. New York, New York: Chapman and Hall. TIC: 218325.

Schelling, F.J. 1989. *DR22-B-In Situ Stress Near ESF.* Albuquerque, NM: Sandia National Laboratories. ACC: NNA.19890523.0038.

Wilder, D.G.; Lin, W.; Blair, S.C.; Guscheck, T.; Carlson, R.C.; Lee, K.; Meike, A.; Ramirez, A.; Wagoner, J.L.; and Wang, J. 1997. *Large Block Test Status Report,* UCRL-ID-128776. Livermore, California: Lawrence Livermore National Laboratory. ACC: MOL.19980508.0727.

5.4 Acoustic Emission/Microseismic Monitoring:

From October, 2000 to June, 2001, no acoustic emission events have occurred. In fact, the last microseism was recorded on July 2, 2000 even though the system has been running continuously since then. Figure 149 shows a bargraph of microseisms per week for the total time the system was operating is shown below. The gap in August, 1999 was due to a power failure cause by a lightning storm which, coincidentally, was also during the time of high seismicity.

The hammer calibration test indicates that energy from the hammer blow can still be detected in the array, but at lower amplitudes for some stations. This suggests that drop off in seismicity is most likely real and not caused by a deterioration in station response, though some smaller events may be undetected due to attenuation of waves caused by the heated rock and/or high temperatures damaging the sensors. The seismicity plots remain the same as August, 2000 (Figures 150-2), since no events have been recorded since then.

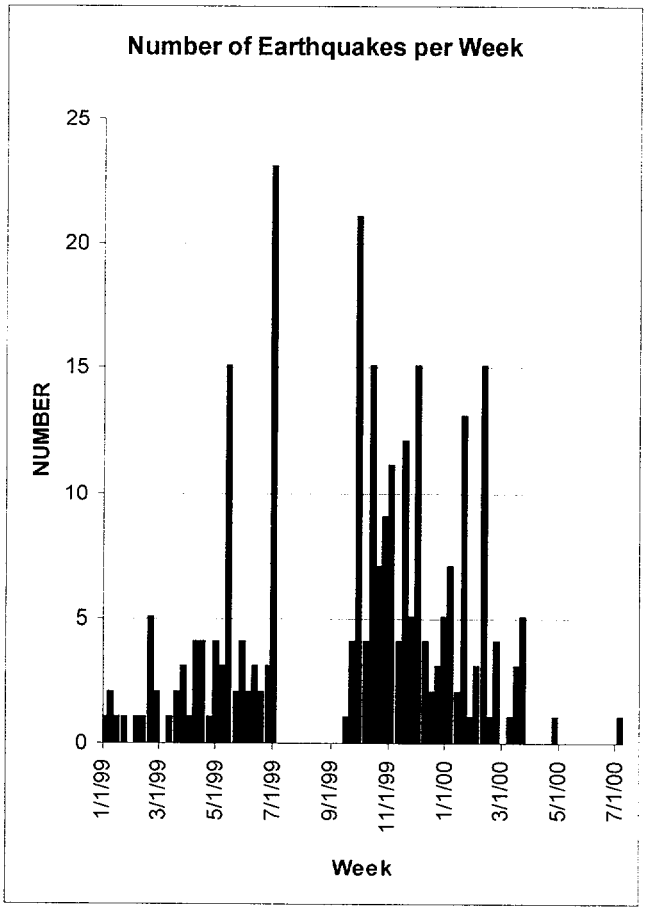

Figure 149. Graph of number of microseisms per week. No events recorded after July, 2000.

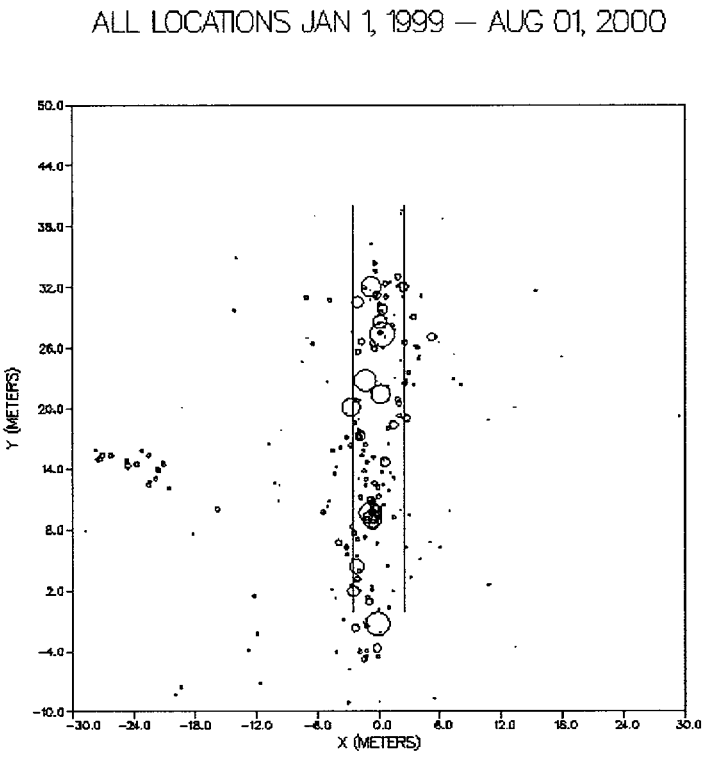

Figure 150. Plan view of microseismicity. The size of the circle indicates that relative magnitude of the microseismic event.

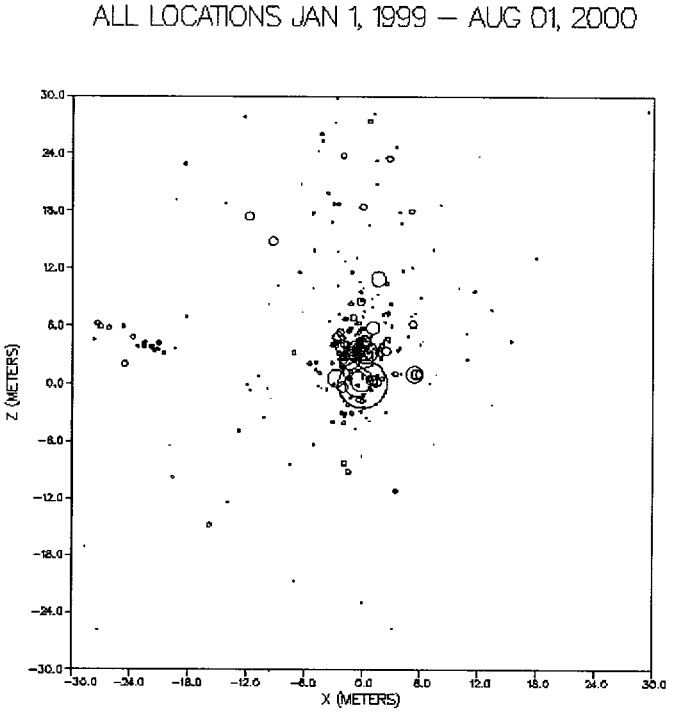

Figure 151. Same as Figure 150 with the events now projected onto the x-z plane. The largest circle at (0,0) represents the Drift.

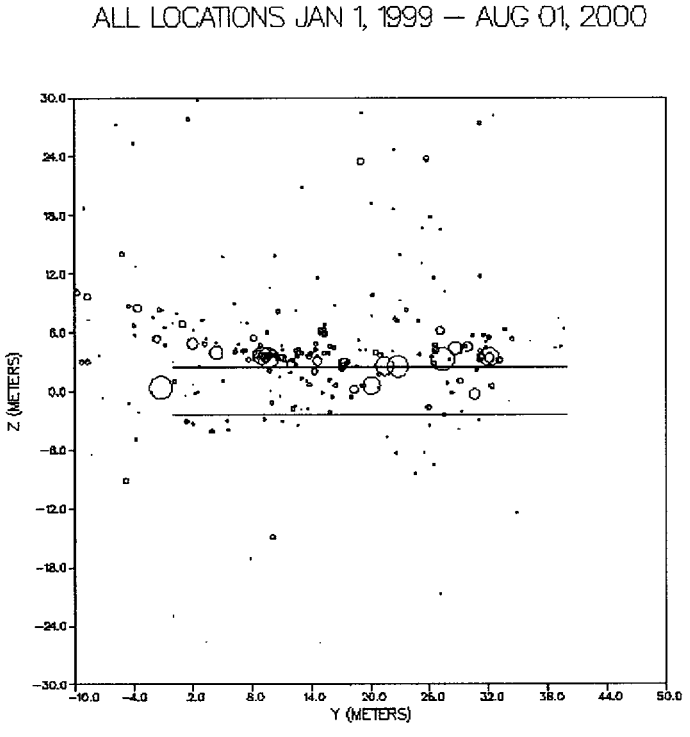

Figure 152. Same as Figure 150 with the events now projected onto the y-z plane.

INTENTIONALLY LEFT BLANK

6. Thermal-Hydrological-Chemical Processes

Chapter 6 includes a discussion of Integrated Assessment of Chemical Measurements and Numerical Analyses.

6.1 Integrated Assessment of Chemical Measurements and Numerical Analyses

6.1.1 Overview

Discussions on geochemistry for the thermal testing program focused on integration of geochemical data and thermal-hydrological-chemical (THC) modeling into Performance Assessment. The four major areas of discussion were: (1) Integration and application of THC models for PA, (2) Gas-phase CO_2 and isotope chemistry, (3) THC model integration and update of THC models with comparison to gas and liquid chemistry, and (4) Sidewall coring mineralogy. Other areas of discussion included the heating schedule for the DST, planning for further geochemical sampling at the DST, and planning regarding the design of the Cross Drift Thermal Test.

6.1.2 Integration of THC Modeling into Performance Assessment

Recently, several major inputs to Performance Assessment and other YMP project documents have been provided based on models of THC processes. Although most geochemical data from the DST are not used directly in the THC models (except for the initial pore water chemistry) the DST remains the most important validation test for the THC models.

The goals of the models used for prediction of drift-scale THC processes and their abstraction are:

- Provide a conceptual basis and methodology for developing drift-scale THC models
- Validate the THC model by comparing its results to results from field (i.e. thermal testing) and laboratory experiments
- Identify conceptual uncertainties and address uncertainty through sensitivity studies that vary key parameters
- Predict changes in hydrologic properties resulting from mineral precipitation/dissolution and associated THC effects on flow and seepage
- Predict changes in water and gas chemistry around drifts, which are the potential elements that could enter drifts through seepage or gas flow.

A list of major project documents where THC modeling and model validation to the DST are discussed is as follows:

- AMR N0120 "Drift-Scale Coupled Processes (DST and THC Seepage) Models" Rev. 01 ICN 01 (BSC 2001)
- UZ PMR
- NFE PMR
- SSPA Volume 1
- NRC KTI - DOE Agreements
- PSSER
- FEPs
- Abstractions for TSPA-SR (seepage water and gas chemistry, effects on flow)

Detailed discussion of the results of the THC models for PA are discussed primarily in the SSPA Volume 1 (Sections 3.3.6, 4.3.6, and 6.3.1) and in AMR N0120 Rev. 01 and are not repeated here. Figure 153 illustrates the general relationship between the DST THC models and geochemical data and the THC models used for PA.

6.1.3. Isotopic Analyses of Gas and Water Samples from the Drift Scale Test

Field Sampling

Two additional sets of gas and vapor condensate samples were collected from the hydrology boreholes since the last thermal test workshop (October, 2000). Analyses of the amount and stable carbon isotopic compositions ($\delta^{13}C$) of CO_2 in the gas samples and the hydrogen (δD) and oxygen ($\delta^{18}O$) isotope compositions of the condensate samples are complete. In addition, most of the analyses of water vapor condensate samples collected during prior sampling periods have also been finished.

CO_2 Data

In general, we have observed that the concentration of CO_2 in the gas samples collected from the DST increase with temperature until the boiling point (~97°C) is reached. Above the boiling point, the concentrations drop off significantly. This is consistent with evolution of CO_2 from the dissolved inorganic carbon (DIC) in the pore water in the rocks during heating up to the boiling point. This is supported by a general trend towards higher $\delta^{13}C$ values as the CO_2 concentrations increase, indicating progressive loss of CO_2 gas (which has lower $\delta^{13}C$ values) from the DIC (which has higher $\delta^{13}C$ values). Once the rock passes through boiling, the pore water is gone and all the DIC has been converted to CO_2 or precipitated in secondary carbonate minerals.

Currently, most of the gas sampling intervals in the DST are above boiling point of water and the CO_2 concentrations are low (<0.2%). However, many of the packers isolating the higher temperature intervals have failed and the gas samples collected from those intervals are a composite of large sections of the monitoring wells. Several of these intervals include sections that are below boiling. As a result, the CO_2 concentrations are considerably higher than expected. For example, the packers separating borehole 78,

interval 3 from intervals 1,2 and 4 are all deflated and the measured CO_2 concentration in 78-3 was 0.8% in April, 2001 despite a temperature of 112°C.

In most of the sampling intervals that are still below boiling, the CO_2 concentrations are continuing to increase (the highest measured concentration in April, 2001 was 7.9% in interval 185-2). The most notable exceptions to this are intervals 74-3 and 75-3 (the two highest intervals above the central part of the heater drift). The CO_2 concentrations have dropped off considerably over the last year. Presumably, this indicates a general depletion of DIC in the pore water in the central area of the heated rock.

Water Vapor Condensate Data

In sampling intervals above 50°C, samples of water vapor condensed from the gas have been collected for hydrogen and oxygen isotopic analyses. Using published relationships between vapor and liquid, we can calculate the isotopic composition of the pore water in the vicinity of the sampling interval from the isotopic composition of the vapor.

Since water vapor has lower δD and $\delta^{18}O$ values than co-existing liquid water, these data provide a measure of the degree of water vaporization and condensation occurring in the area of the sampled interval. In general, we have observed that the isotopic composition of the pore water remains approximately equal to the initial $\delta^{18}O$ value of the pore water (–11‰) up to ~90°C. Once the temperature approaches the boiling point, the degree of vaporization of the pore water becomes significant and the isotopic values increase. Exceptions to this include areas where condensed water vapor has been added to the pore water, either by draining through fractures (e.g., beneath the drift in intervals such as 78-3) or where water vapor generated in the boiling zone condenses in the rock above the boiling front and mixes with the pore water (e.g., interval 75-3). In these cases, the low-$\delta^{18}O$ condensate causes the overall isotopic composition of the pore water to decrease. These effects are demonstrated by the data plotted in Figure 154. The oxygen isotopic composition of the pore water around interval 59-3 is equal to or slightly lower than the –11‰ until the temperature in the interval exceeds 93°C. Then the $\delta^{18}O$ value of increases to approximately –6‰ as the rock dries out. In interval 58-3 (~4 m above 59-3), the $\delta^{18}O$ value of the pore water is about –11‰ until the condensate from the boiling front begins accumulating in the rock and the $\delta^{18}O$ value of the pore water drops to approximately –14‰.

6.1.4. DST THC Model Updates and Comparison to New Data

Since the last thermal test workshop, the DST THC model has undergone minor updates, and comparisons to several measurements of water and gas chemistry wee presented in the previous thermal test workshop progress report. No new water chemical data were available at the time of the workshop and therefore no further comparisons are made here. Hence, the discussion on DST THC model results focuses primarily on comparison to the recently collected gas phase CO_2 data.

As discussed in Section 3.2, many of the gas-phase CO_2 analyses are from intervals above the boiling temperature where the packers have been deflated. Thus, these CO_2 data are no longer directly comparable to model results because they represent mixtures

of gas from a long interval that crosscuts zones of widely differing temperatures and liquid saturations. Therefore, modeled and measured CO_2 concentrations are shown for only for two borehole intervals (borehole 74, interval 3, and borehole 75, interval 3) where the packers are still intact. For reference, the locations of these borehole intervals and the model grid nodes are shown in Figure 155.

Figure 156 depicts models results from model grid nodes on both the hotter and cooler sides of borehole 74 interval 3, as there are no grid nodes near the center of the interval. The last measured data points (January and April 2001) were determined using a standard concentration that yields values about 15% higher than the previous samples, and although they appear to show nearly constant CO_2, are actually relatively lower in concentration than those collected previously. A consistent recalibration of all the CO_2 concentrations will be done to make the analyses directly comparable. Considering that the earlier analyses should be somewhat higher, the trend in measured compositions is quite similar to the average trend of the model concentrations, that can be inferred from the individual trends. The main difficulty in capturing the later time trend is that the concentrations in the hotter interval are dropping rapidly, whereas those in the cooler interval have only begun to level out.

Measured and modeled CO_2 concentrations from borehole 75 interval 3 are shown in Figure 157. Here the modeled concentrations closely capture the magnitude and trend in concentrations observed up to April 2001. Both results show the strong depletion in CO_2 as the boiling front is advancing toward the interval and as the matrix pore waters are stripped of CO_2 through vaporization and transport to cooler areas.

6.1.5 Mineralogic Analysis of Drift Scale Test Sidewall Cores

In November, 2000, a new sidewall coring tool was used to collect six sidewall cores from inclined boreholes 53 (ESF-HD-CHE-2) and 54 (ESF-HD-CHE-3) while the thermal test was in progress. This capability is a significant improvement over the sampling options for the Single Heater Test, in which overcore samples were collected for mineralogic analysis only after the block had cooled down.

Target Selection

The target locations for sampling were selected on the basis of thermal data and predictions and examination of borehole televiewer logs. Borehole intervals with visible fracturing were chosen to maximize the likelihood of finding mineral deposits resulting from water-rock interaction during the test. The locations targeted for sampling in borehole 54 are within the boiling zone as it existed in November, 2000. It is important to note that these locations existed within the condensation zone above the boiling zone until the boiling zone moved outward to intersect borehole 54, so that observed test effects may be composites of condensation-zone and boiling-zone processes. Borehole 53, higher in the test block than borehole 54, is in the condensation zone and has not experienced temperatures at or above boiling.

Sample Recovery

Six core samples were collected during the inaugural deployment of the sidewall coring tool. The recovered cores received a preliminary examination by stereomicroscopy. Two of the samples from borehole 53 were test targets chosen to evaluate tool performance and were essentially outside the zone of thermal test influence. One such sample contained a natural fracture with no obvious evidence of new mineral deposition. The other sample included a portion of the pre-test wellbore surface, also without evidence of new mineral deposition. These two samples were assigned the lowest priorities for further characterization. A third sample from the condensation zone intersected by borehole 53 also contained only a portion of pre-test wellbore surface without evidence of mineral deposition. This sample was assigned low priority for further characterization, and none has yet been done.

The three samples from borehole 54, collected in two locations where the borehole intersects the boiling zone, all contain evidence of mineral deposition related to the test. The most easily visible deposit is glassy silica scale. One sample also contained minute white, fibrous rosettes of an additional mineral; this sample was selected for detailed examination by scanning-electron microscopy (SEM). For comparison, a sample of pre-test drill core containing a fracture from about the same depth was studied by SEM to provide a baseline inventory of pre-test fracture mineralogy and mineral textures. Chemical compositions of minerals were determined semi-quantitatively by energy-dispersive x-ray spectroscopy.

Basis for Interpretation of Mineral Deposits

The identification of particular mineral deposits as products of water-rock interaction during fluid reflux in the condensation zone, evaporation in the boiling zone, or composites of reflux and evaporation is a matter of interpretation. Salts like calcium carbonate and calcium sulfate are interpreted as products of substantial evaporation. We know that these compounds were deposited in the condensation zone of the Single Heater Test at temperatures below boiling, probably when the rock began to dry out after test completion. This combination of conditions did not exist at sampling time in either the boiling or condensation zones of the Drift Scale Test, and therefore we expect salts to be deposited in the boiling zone and to be products of high-temperature evaporation during dryout.

It is not clear what deposits from the condensation zone might look like. It seemed likely that conductive fractures would receive numerous packets of reflux water and that mineral deposits, probably silica, would have textural features reflecting multiple episodes of deposition. For example, a deposit built up from many layers of silica or built by aggregation of many smaller deposits could be a product of deposition in the condensation zone.

Silica deposits produced only by evaporation in the boiling zone are expected to be thin, with little or no indication of successive buildup. Deposits were expected to be thin because any particular portion of fracture surface would receive deposition only from evaporating water exiting the adjacent rock matrix.

Pre-Existing Natural Fracture Minerals

Pre-test core samples from the depths where sidewall samples were collected were analyzed for natural fracture mineralogy. The natural mineralogy is the baseline for documenting evidence of mineralogic change in fractures during the test. Potential changes during the test might include deposition of new mineral phases and dissolution of pre-existing minerals. In several cases, the pre-test core samples were collected from slightly different depths than the sidewall samples because core at the precisely corresponding depth contained no fractures and therefore was unsuitable for analysis. Some information about pre-existing natural fracture minerals was also obtained from examination of sidewall samples.

The dominant fracture-coating mineral from pre-test core ESF-HD-CHE-3 (hole 54) at the 66.7-ft depth is the calcium zeolite stellerite. Additional minerals include potassium feldspar, crystalline silica, smectite, mordenite, and minor pyrite. The rock matrix exposed on some parts of the fractures is mostly a fine-grained mixture of feldspar and silica minerals.

Test-Related Mineral Deposition

The three products observed so far are tentatively identified as amorphous silica, a calcium sulfate phase (gypsum or anhydrite), and a calcium-rich phase that is probably calcite. The silica deposits exhibit considerable textural heterogeneity, perhaps because some were deposited when the collection site was in the condensation zone and others deposited when boiling-zone dryout conditions were reached.

The images in Figure 158 (file 3) and Figure 159 (file 9) show two examples of possible condensation-zone silica deposits. Figure 158 shows a fracture surface completely coated by terrace-like silica deposits up to a few micrometers thick. In Figure 159, several discoid silica deposits (up to about 20 micrometers across) rest on a surface of earlier-deposited discs cemented and largely obscured by silica particles about one or two micrometers across. In both examples, the deposits were built up during multiple episodes of silica deposition.

Very thin (less than 0.5 micrometer thick), curled silica sheets may be products of final dryout in the boiling zone, Figure 160 (file 17). There is no textural evidence of successive buildup in the silica sheets. Also lying atop the earlier silica deposits or on pre-test fracture surfaces are scattered deposits of prismatic calcium sulfate Figure 161 (file 16) and rounded mounds of probable calcite Figure 162 (file 11).

Evidence of Dissolution

Possible dissolution of natural fracture-coating minerals was observed adjacent to one of the thicker lobate silica deposits interpreted as condensation-zone deposits, Figure 163 (file 4), Figure 164 (file 10). A highly corroded stellerite crystal Figure 164, (pt 2) presents a strong textural contrast to the well preserved prismatic crystal forms away from the silica deposit. Next to the corroded stellerite, a silica crystal, probably cristobalite, also appears corroded Figure 164 (pt 1). The localization of dissolution

evidence close to test-related silica deposits suggests that much of the dissolved material is redeposited after very little transport.

6.1.6 Planning for Further Sampling at the DST

Suggestions were made regarding the potential for collecting water in the future. Based on the lack of significant water collected from boreholes and the slow rate of advance of the boiling front it does not appear likely that samples will be collected from the upper hydrology boreholes (e.g., boreholes 58 and 75). Therefore, another potential way of collecting pore water was proposed. This involves drilling through regions of high liquid saturation where matrix inbibition of draining fracture waters has taken place. Direct measurement of liquid saturation will enable estimates of fracture-matrix interaction. Additionally, ultracentrifugation of the pore waters will allow for assessment of matrix pore water dilution as well as give constraints on water-rock interaction.

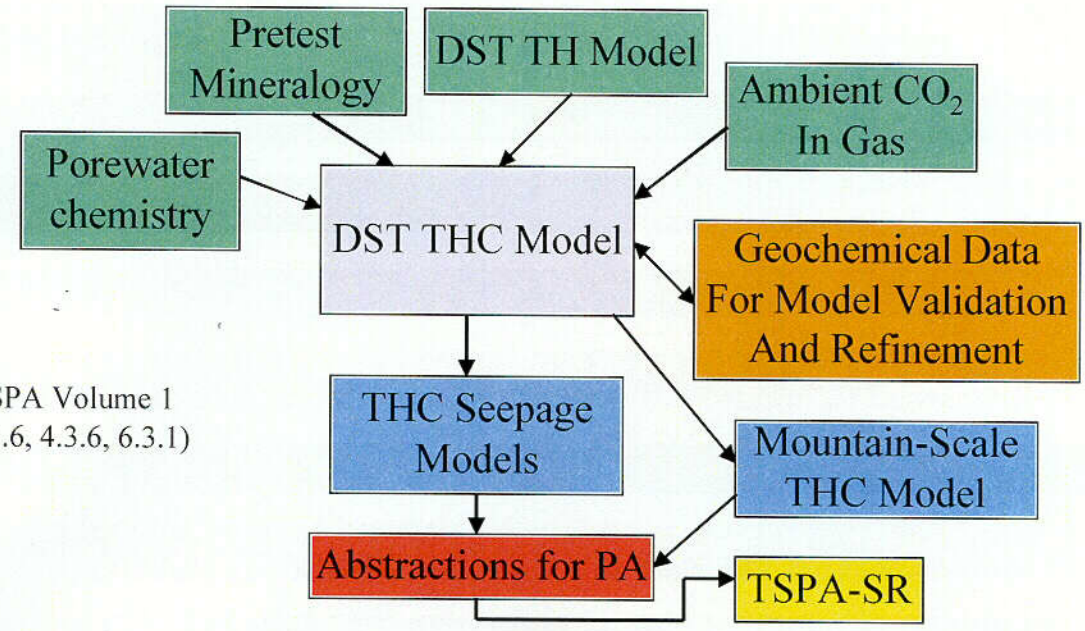

Figure 153. DST THC data, model, and integration into PA.

C17

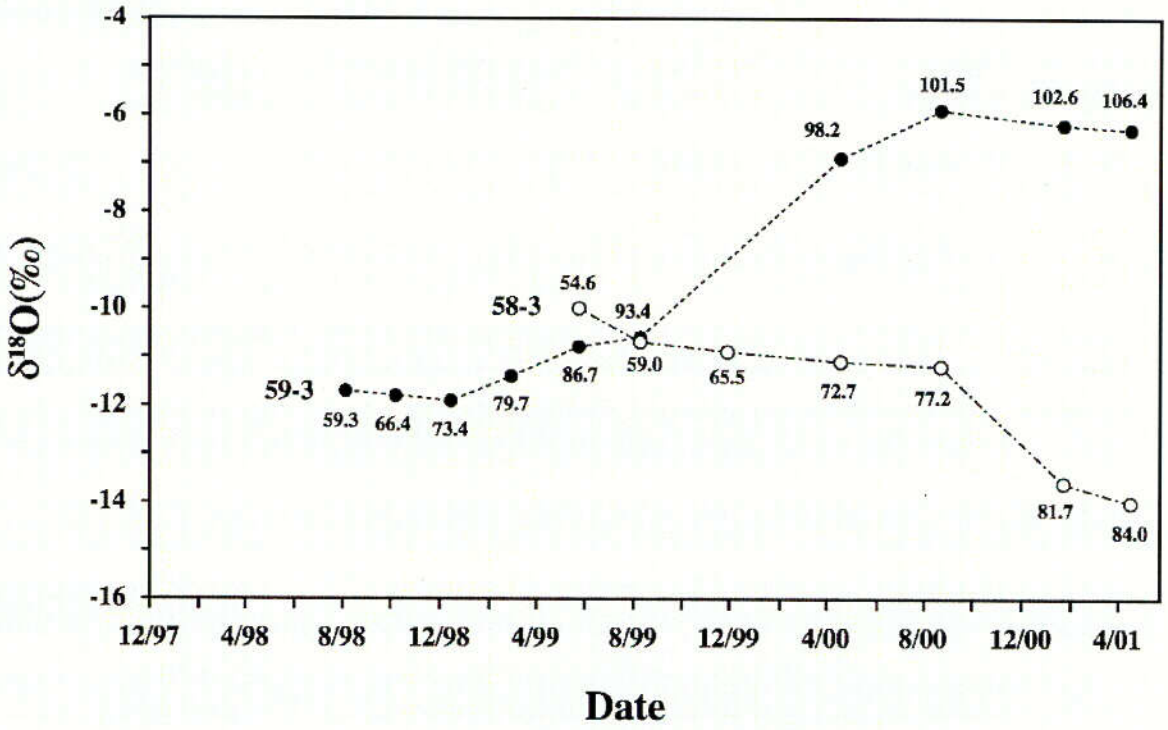

Figure 154. $\delta^{18}O$ values of vapor condensate (re-calculated to represent the oxygen isotope ratio of water in equilibrium with the vapor) collected from interval 3 in boreholes 58 and 59. Also shown are the temperatures (°C) for the intervals at the times the samples were collected.

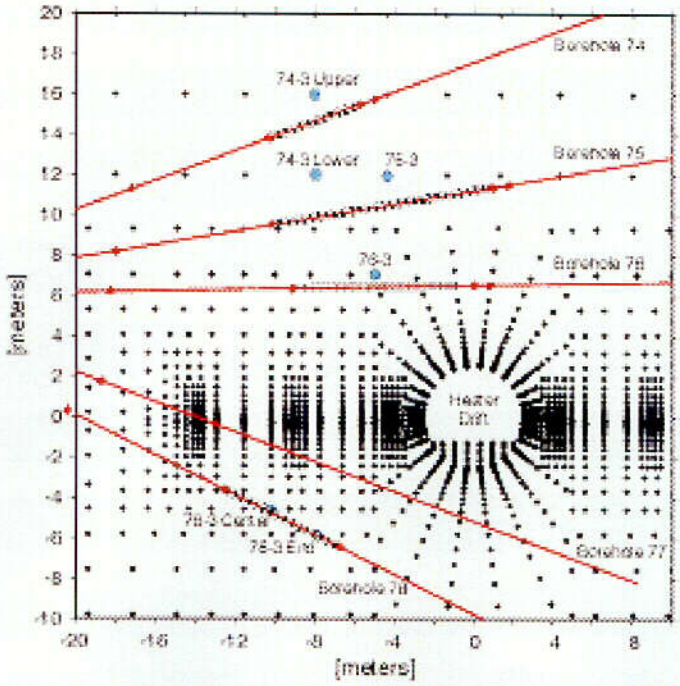

Figure 155. Layout of borehole intervals and DST THC model grid nodes. Colored nodes refer to those used for comparison to CO_2 concentrations.

C18

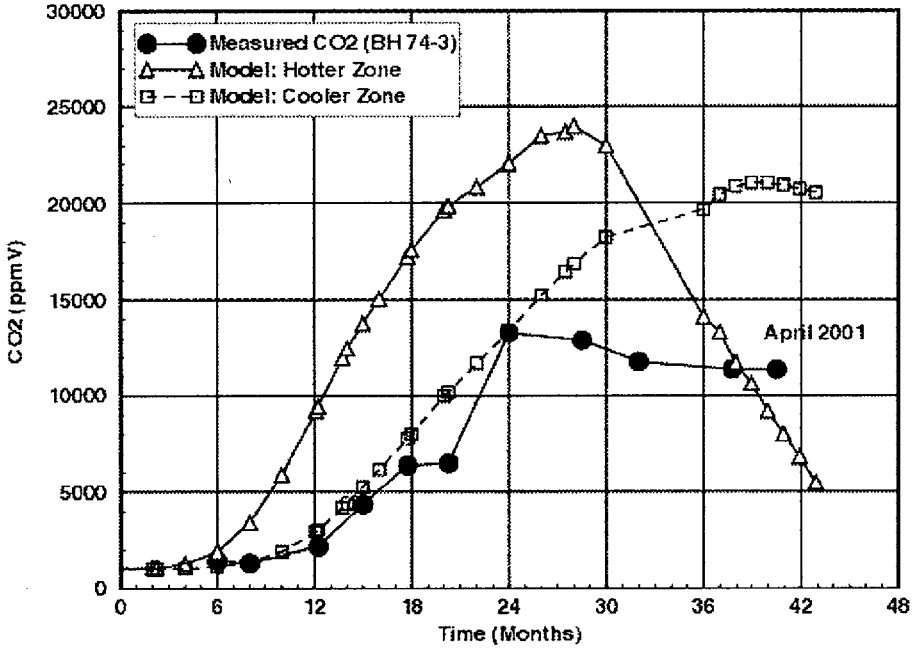

Figure 156. Evolution of measured CO_2 over time from Borehole 74, interval 3 compared to DST THC model results. As a result of coarser discretization in the area of this interval, model results from elements on the hotter and cooler sides are shown.

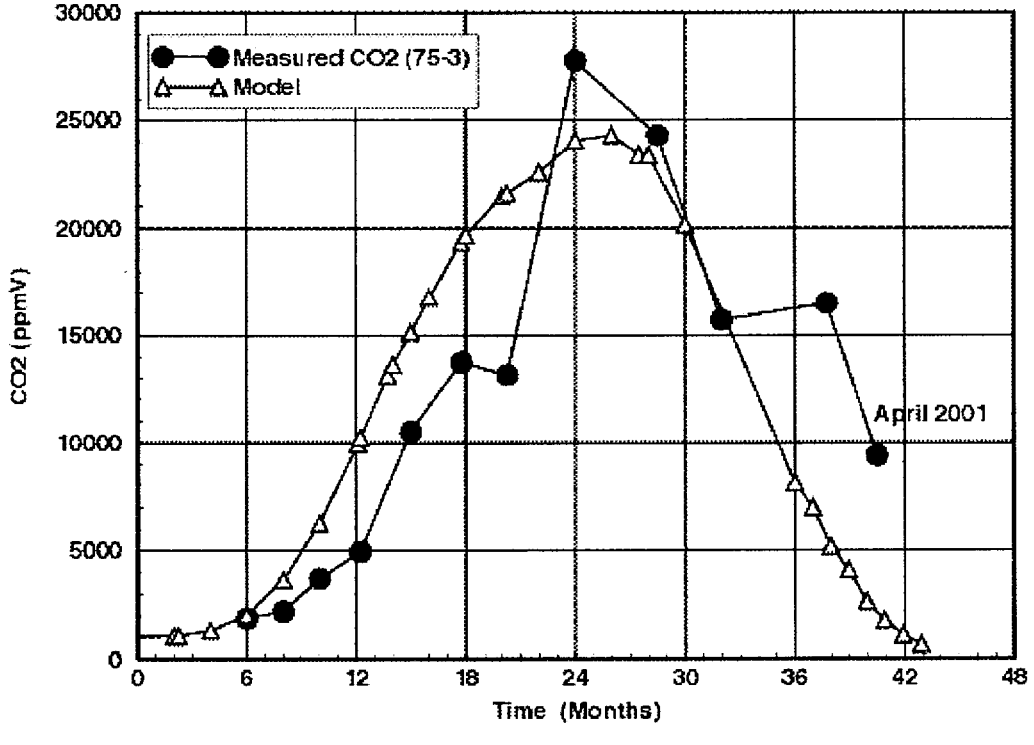

Figure 157. Evolution of measured CO_2 over time from Borehole 75, interval 3 compared to DST THC model results.

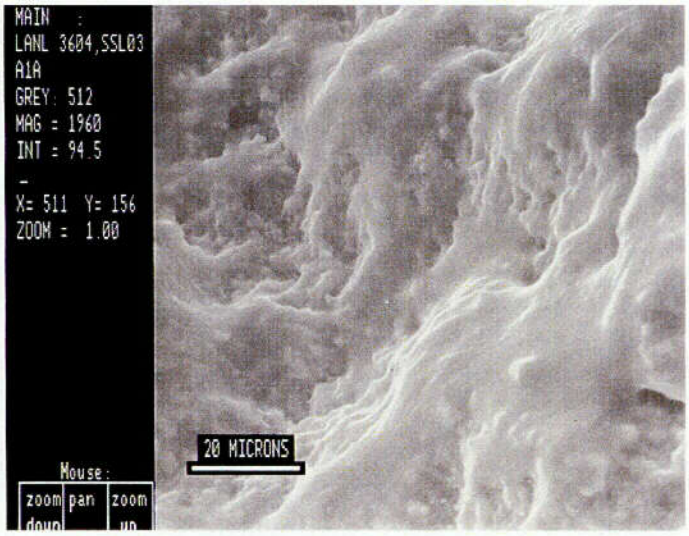

Figure 158 (file 3) Terrace-like deposits of amorphous silica coating a fracture surface. Secondary-electron image.

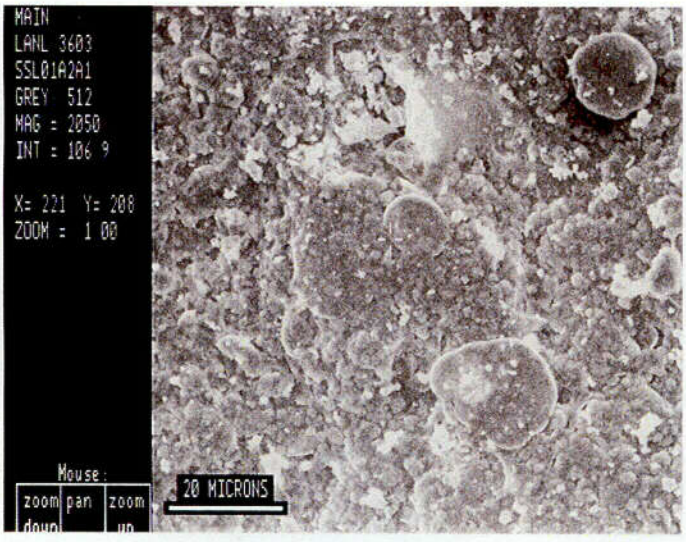

Figure 159 (file 9). Discoid silica deposits rest on a surface of earlier discs cemented by silica particles. Secondary-electron image.

C19

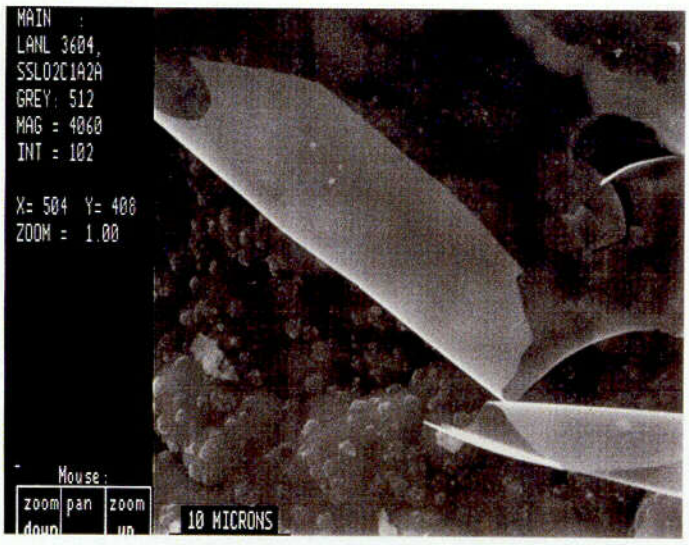

Figure 160 (file 17) Curled sheets of amorphous silica atop a small depression coated with earlier silica. Secondary-electron image.

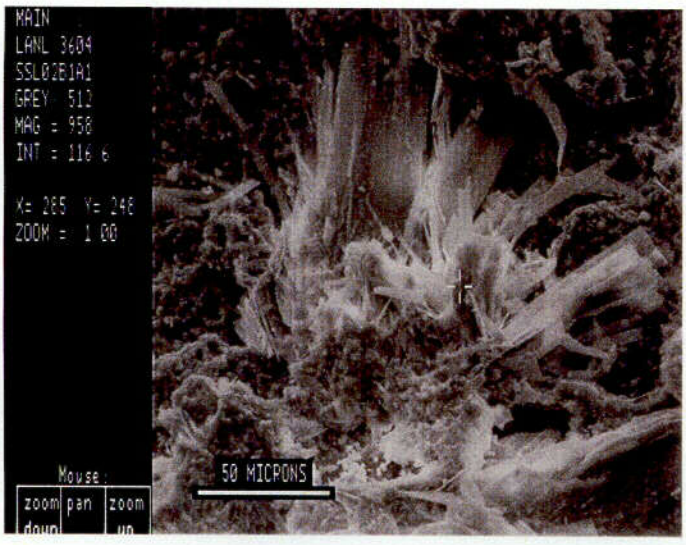

Figure 161 (file 16) Prismatic calcium sulfate. Secondary-electron image.

C20

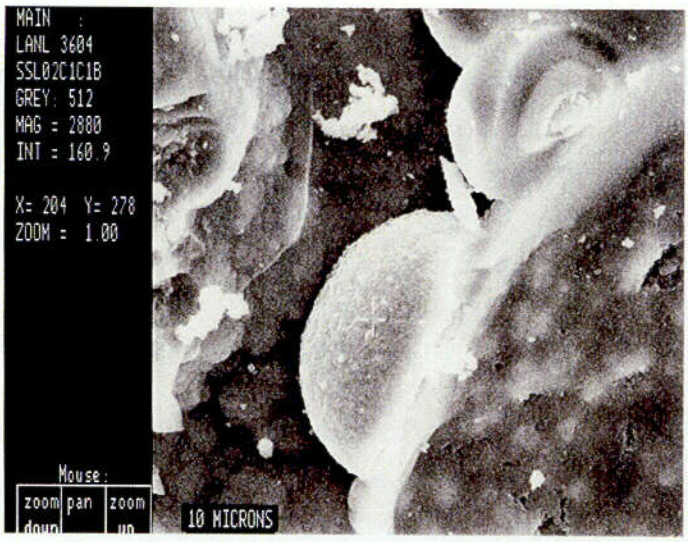

Figure 162 (file 11) Rounded mounds of probable calcite atop an earlier silica deposit. Secondary-electron image.

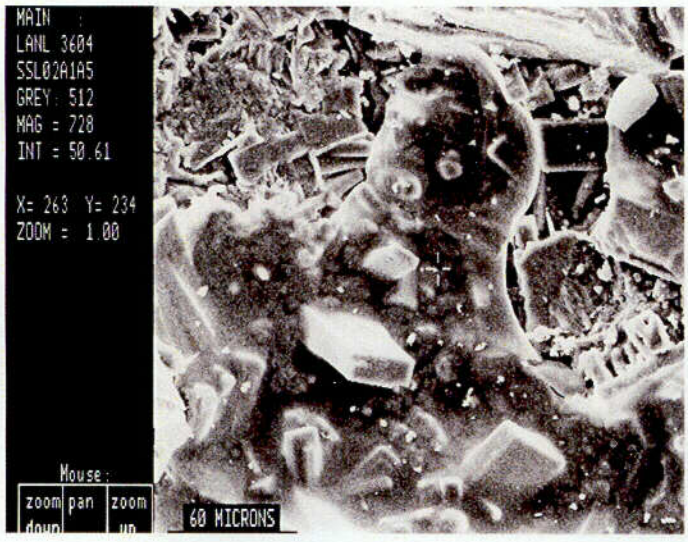

Figure 163 (file 4) Prismatic stellerite and other pre-test minerals engulfed by a lobate deposit of amorphous silica. Secondary-electron image.

C21

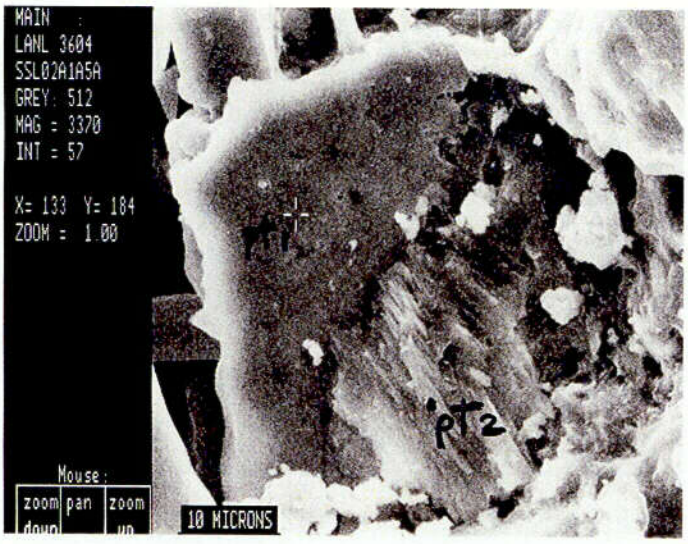

Figure 164 (file 10) Corroded pre-test crystals of stellerite (pt 2) and silica (pt 1) adjacent to the lobate deposit in Figure 163 (file 4). Secondary-electron image.

C22

INTENTIONALLY LEFT BLANK

7. Drift Scale Test Heating/Cooling Schedule Revisited

Discussions were held during the June 8, 2001 workshop regarding the heater shut-off for the Drift Scale Test. Results from recent thermal calculations were presented that predicted heated drift wall temperatures of about 80 degrees C after 3 years of cooling. These predicted temperatures are shown in Figure 25.

Principal Investigators representing each of the three coupled process models presented their opinions. No one advocated extending the heating phase beyond the original 4 year plan. The Thermal-Chemical Process group requested 1 or 2 new core boreholes to investigate fluid reflux in the boiling zone shortly after shut-off. The Thermal-Mechanical group was interested in installing 5 tiltmeters in boreholes surrounding the heated drift. Tilitmeter boreholes would measure small movement in the rock following heater shut-off.

Drift Scale Test heater shut-off is a level 2 milestone as defined by the baseline plan. Unless preempted by new test information, workshop participants agreed that complete heater shut-off should proceed as originally planned with a slight delay to the beginning of 2002.

INTENTIONALLY LEFT BLANK

8. Planar Heat Source Design for the Cross Drift Thermal Test (CDTT)

The current design of the CDTT involves a planar heat source consisting of 11-rod heaters placed in parallel and spaced at 0.8 meters as shown generally in Figure 165. A 12^{th} rod heater, parallel to the others, will be placed at 4.5 meters from one edge of the planar heat source. The current design should meet the same objectives as listed on page 6, Section 2.0 of the Cross Drift Thermal Test Planning Report published last August 2000. In addition to the broad objective of acquiring a better understanding of the coupled thermal-hydrological-mechanical-chemical processes in the near field of the lower lithophysal unit of Topopah Spring welded tuff, Section 2.0 of the planning report also listed a prioritized set of specific objectives. I shall address them one by one to show that not only have none of the stated objectives been compromised by the current design, but the THC aspect of the test objectives have been strengthened.

1. To test or investigate the premise that heat-mobilized pore water will shed/drain between emplacement drifts to below the repository horizon.

This objective will be met by the design of the 12^{th} rod heater, and the horizontal drainage monitoring (temperature and neutron logging) boreholes placed at mid-point of 11^{th} and 12^{th} heater. The 12^{th} heater is far enough away from the edge of the planar heat source so that the monitoring borehole will indeed be monitoring the drainage "between drifts". Another horizontal drainage monitoring borehole will be placed at within one meter of the 11^{th} heater; this borehole will measure the drainage/shedding from the "repository edge". The heating power in 12^{th} will be adjusted (based on TH modeling) to give rise to temperature gradient that is symmetrical about the mid-point of 11^{th} and 12^{th} heaters.

2. To test or investigate the premise that liquid water can penetrate through zones/regions at or above boiling temperature.

This objective is met by the design of the two temperature/neutron boreholes that have closely spaced temperature sensors between the elevation of the heater plane to 2.5 meters above the heater plane. Downward spikes of temperature from above boiling will be indicative of water penetrating through. The current design relies on temperature signatures for occurrence of water getting through. Temperature is the most sensitive measure, more so than geophysical measurements (which are volume averaged measures), and far more reliable that actual collection of water. This latter is because collection boreholes act as capillary barrier, therefore water collection in a borehole is only possible if there are local areas of full liquid saturation around the borehole. This is not very likely since drainage may increase the liquid saturation in the fractures only slightly. If water is not collected in the borehole it does not mean that drainage will not occur.

2 To measure the rock mass properties of the Tptpll.

This objective is not affected by the change of heat source design.

3 Chemistry of seepage water.

One of the motivation for changing the heat source to the current planar design is to ensure that there will be "prolonged" period of stable two-phase zone to insure that there can be repeated sampling of water. The placement of the three water collection boreholes at heights of 1.25 m, 2.0 m and 2.5 meters above the heater plane are at optimum elevations within these two-phase zones through the duration of heating.

4 Chemistry of gas.

This objective is not affected by the change of heat source design. The current plan also calls for sampling gas from the heater boreholes.

In summary, the current CDTT retains the objectives put forth in the planning document published August 2000. The modified design makes the test more efficient in construction, installation and implementation, and we are more likely to succeed in obtaining crucial data prior to LA.

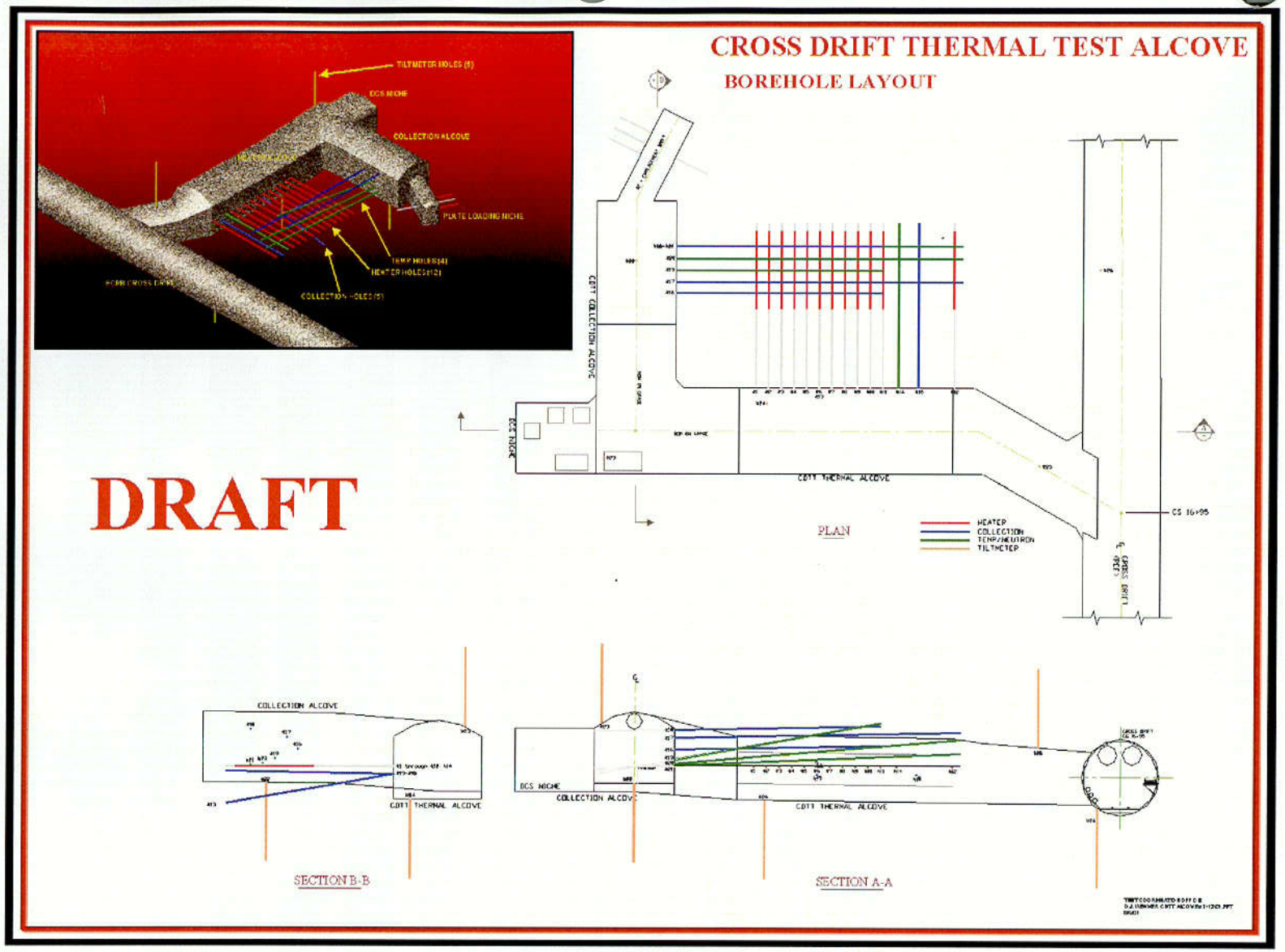

Figure 165. Preliminary Cross Drift Thermal Test Alcove Borehole Layout

C23

INTENTIONALLY LEFT BLANK

9. DECOVALEX

9.1 GENERAL

DECOVALEX is an international consortium of governmental agencies associated with the management/disposal of high level nuclear waste and spent nuclear fuel in Canada, Germany, Japan, Finland, France, Spain, Sweden, the United Kingdom, and the United States. DECOVALEX stands for **DE**velopment of **CO**upled models and their **VAL**idation against **EX**periments, coinciding with the overall objective of the consortium. Simply stated the objective of DECOVALEX is validation of models which can be used to simulate thermal-hydrological-mechanical processes in the rock surrounding a nuclear waste repository.

DECOVALEX I, the first DECOVALEX project was from 1992 to 1995. The U.S. Nuclear Regulatory Commission was a participant in DECOVALEX I. DECOVALEX II was from 1995 to 1999. Both the Department of Energy's Yucca Mountain Site Characterization Office and the U.S. Nuclear Regulatory Commission joined DECOVALEX III which was started in 1999 and is expected to continue till 2002. In DECOVALEX III the Drift Scale Test at Yucca Mountain, which is a large scale, long term in-situ heater test, is a test case.

There are four tasks in DECOVALEX III. Task 1 is on the FEBEX test which is an engineered barrier system in-situ thermal test being conducted at the Grimsell site in Switzerland. The FEBEX test, sponsored by several European governmental agencies, is operated by ENRESA of Spain. Task 2 is on the YMP Drift Scale Test. Task 3 is on several topics such as coupled THM processes due to glaciation and homogenization or upscaling etc. Task 4 is a forum for DECOVALEX participants to interact with invited PA experts on the application of THM models in performance assessment.

The YMSCO is a participant in Task 1 and leads Task 2. It is also a participant in the BMT2 sub-task of Task 3. BSC provides technical support services on DECOVALEX including coordination of all activities and leading Task 2 studies. Currently, Task 1 modeling and analyses are assigned to Sandia National Laboratories, while Task 3 (BMT2) modeling and analyses are assigned to Lawrence Berkeley National Laboratory.

9.2 ACTIVITIES SINCE TOKAI WORKSHOP

Since the third DECOVALEX workshop was held in Tokai in January 2001 there was a Task 1 taskforce meeting in Madrid, Spain on May 22, 2001. Steve Sobolik of SNL attended this taskforce meeting. SNL have been doing simulations of laboratory-scale oedometer tests with Bentonite. SNL has also been developing a coupled version of the TOUGH2 and JAS3D codes.

On Task 2, BSC recently prepared the first draft of the Task 2A Interim Report and circulated it to Task 2A research teams for review. Task 2A Interim Report is expected to be completed by the time of the next workshop in Naantali, Finland in October 2001.

LBNL is currently performing phase II calculations on BMT2 and will present and discuss the results in the next workshop.

APPENDIX A

Drift Scale Test Index Figures and Information

This appendix contains index figures of test layouts, borehole configurations, and other general information familiar to the researchers but perhaps not familiar to all readers. It is important for the reader to understand that individual contributions contained herein may report locations in slightly different ways.

Boreholes may be referred to by one of two unique names: their numerical sequence number or by their functional sequence number. Table 1 of this appendix includes a list of boreholes numbers and names along with collar and bottom coordinates.

A local coordinate system has been established for each of the thermal tests to date. The DST coordinate system is shown in Figure 1 of this appendix. The 0,0,0 point is at the center of the heated drift bulkhead. The (0,0,0) coordinate for the DST is at: North 234,059.947, East 171,431.994, Elev. 1052.855 in Nevada State Plane Coordinates. The positive X axis extends approximately 18 degrees east of north and the positive Y axis extends 72 degrees west of north.

Another common data reporting method uses the distance along a borehole as measured from the collar of the borehole. Boreholes are generally oriented parallel to one of the axes of the coordinate system

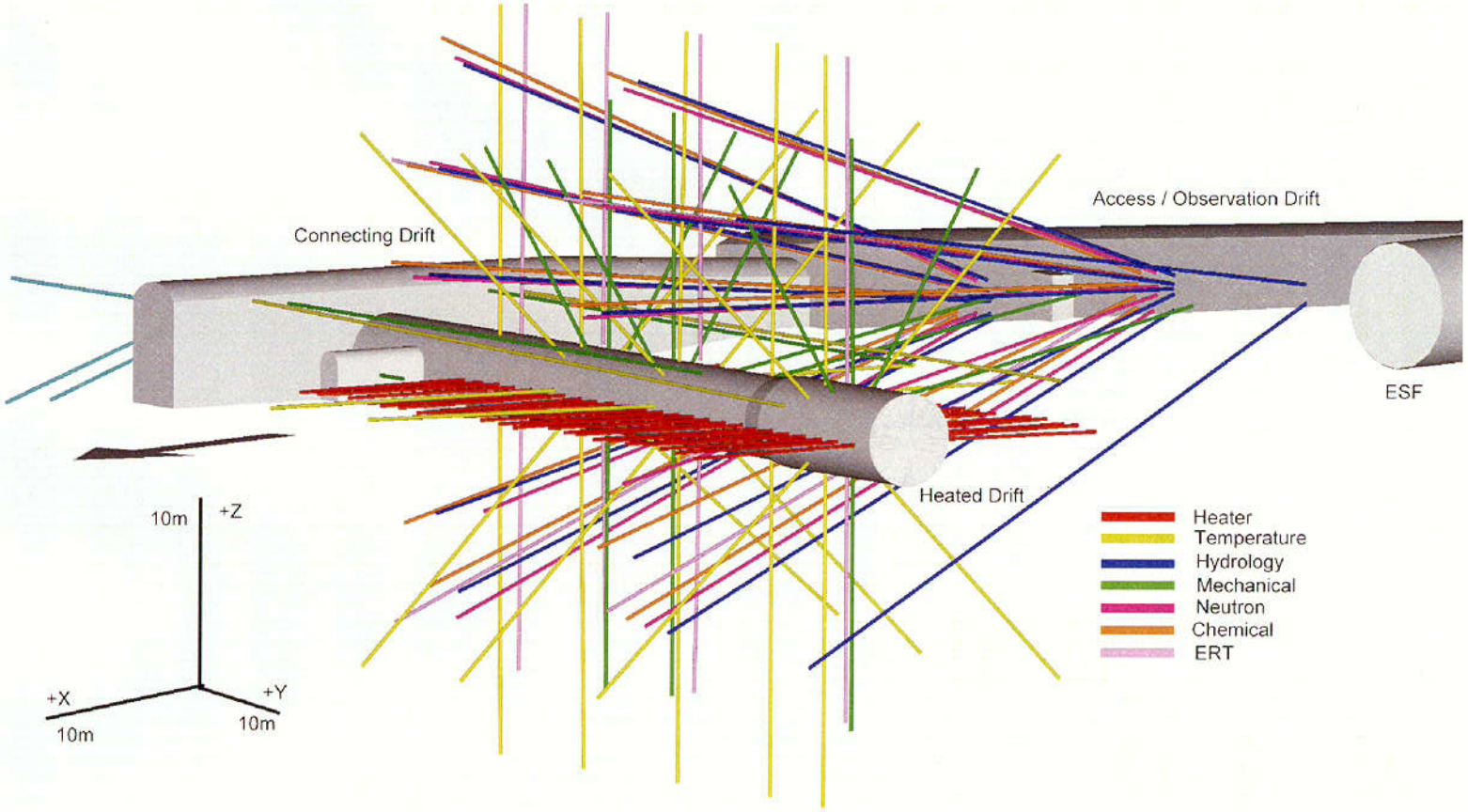

Figure 1. Perspective View Showing Drifts and Boreholes of the Drift Scale Test.

C24

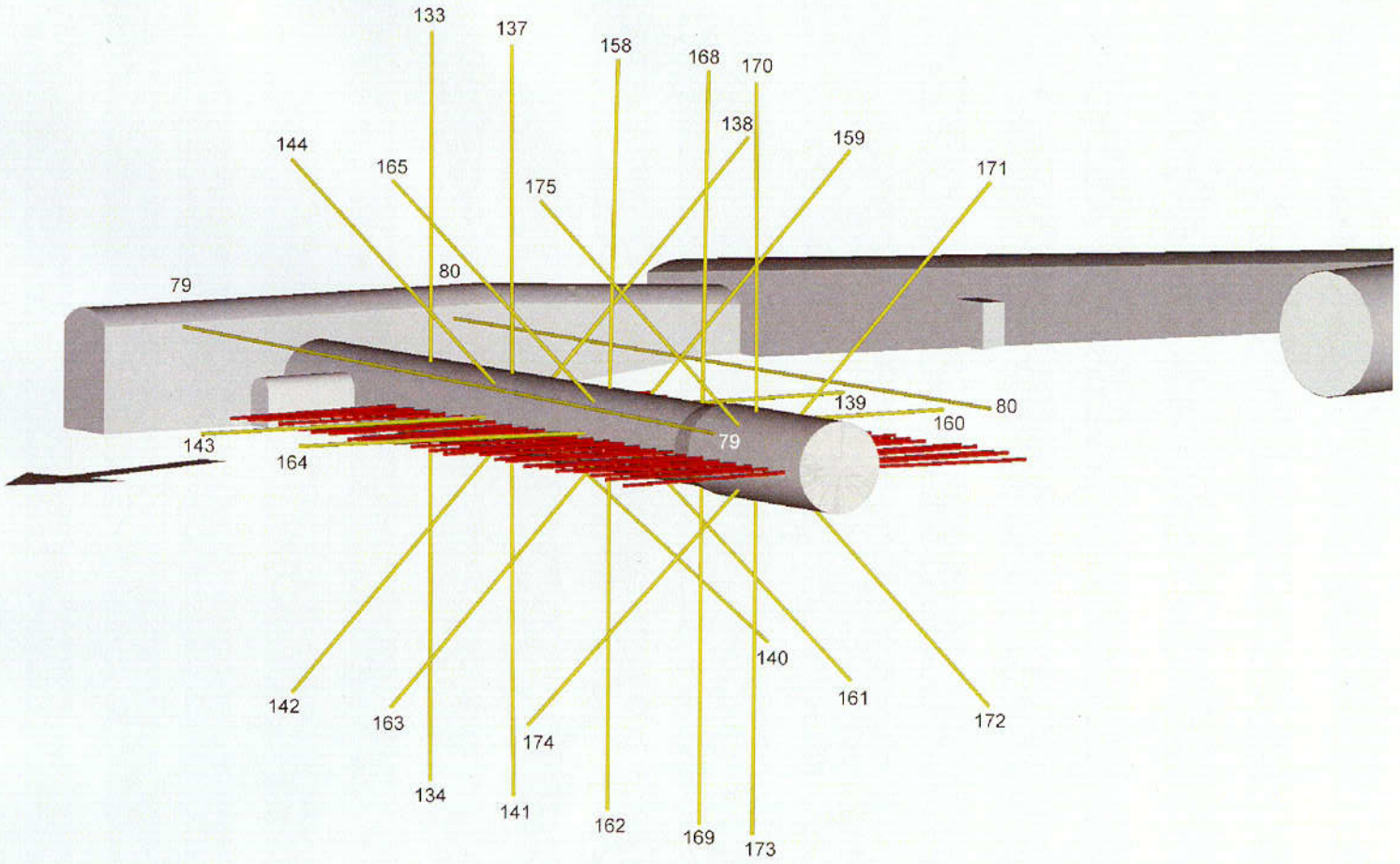

Figure 2. Perspective View Showing Temperature (RTD) Boreholes of the Drift Scale Test.

C25

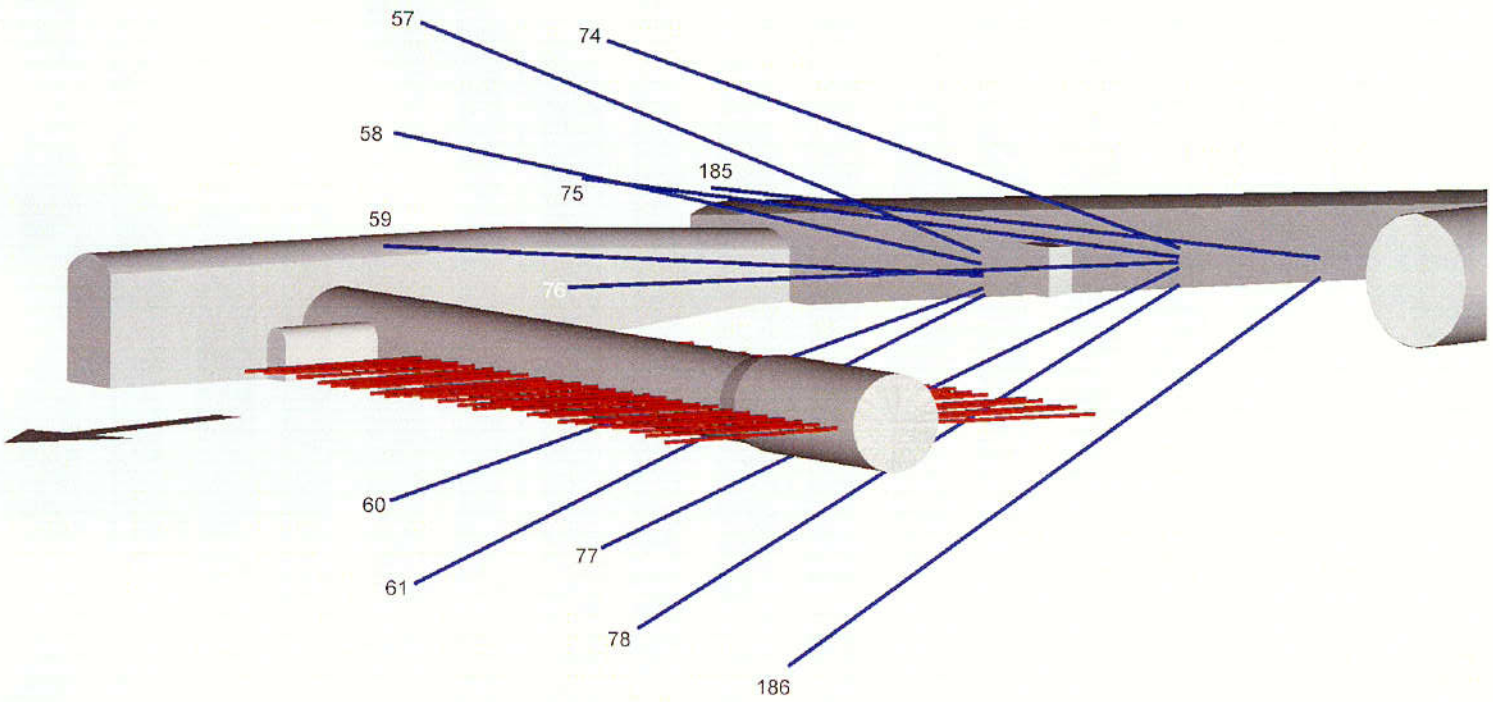

Figure 3. Perspective View Showing Hydrology Boreholes of the Drift Scale Test.

C26

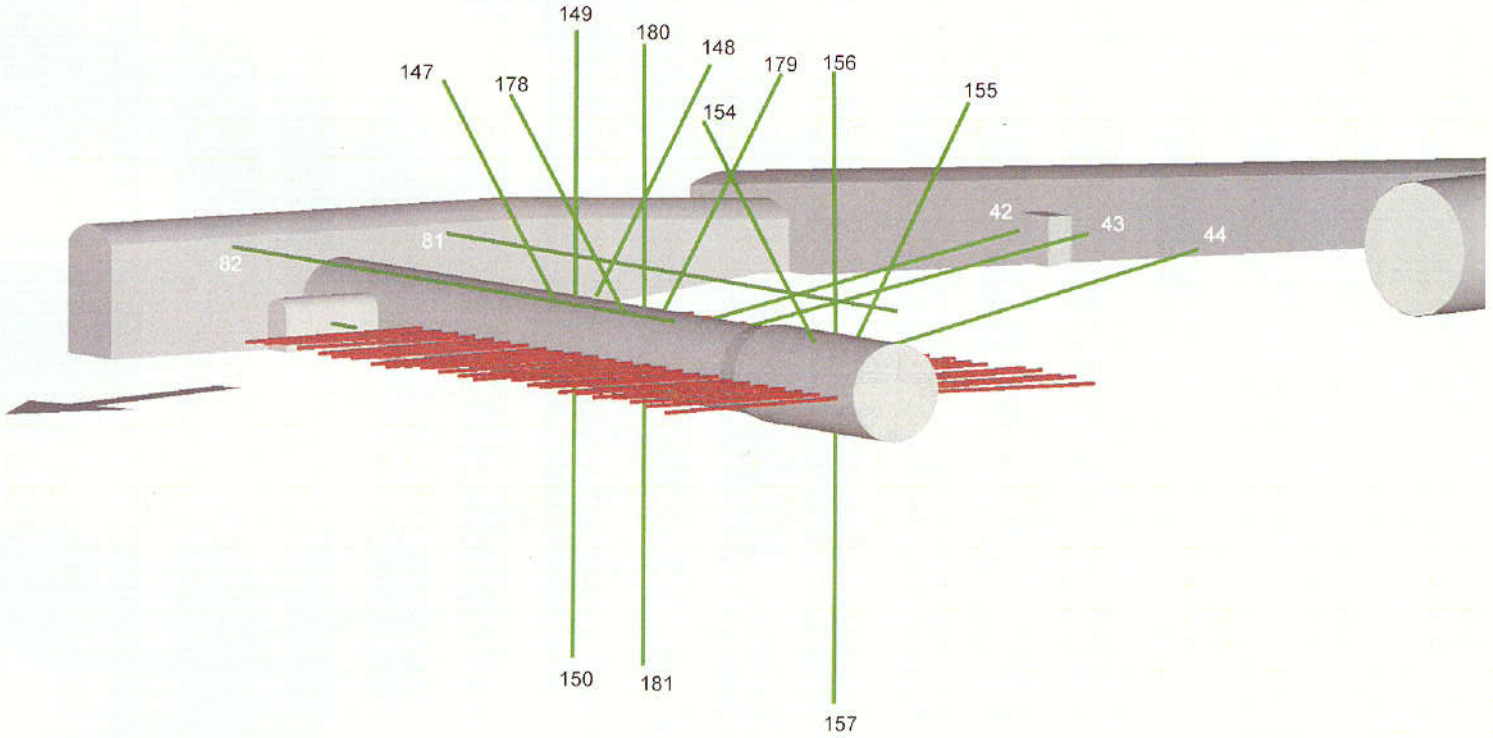

Figure 4. Perspective View Showing Mechanical (MPBX) Boreholes of the Drift Scale Test.

C27

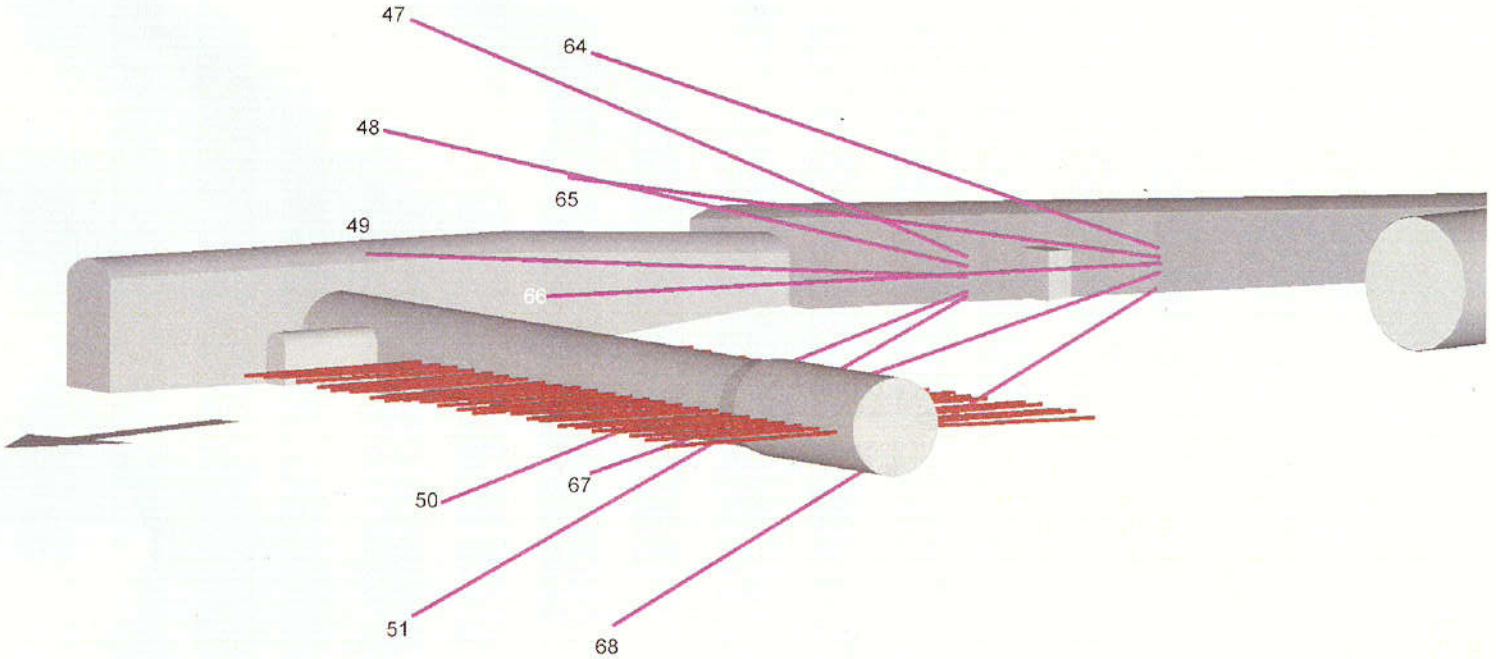

Figure 5. Perspective View Showing Neutron Boreholes of the Drift Scale Test.

C28

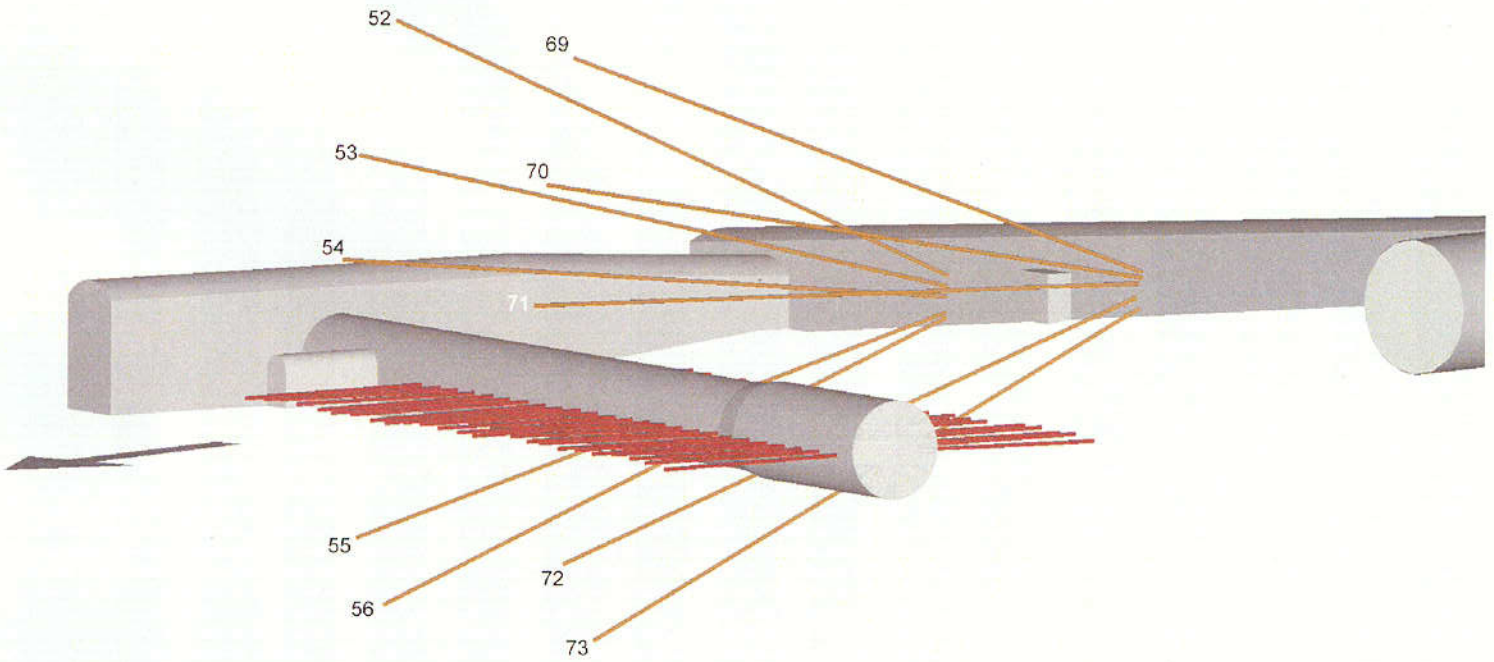

Figure 6. Perspective View Showing Chemical (SEAMIST) Boreholes of the Drift Scale Test.

C29

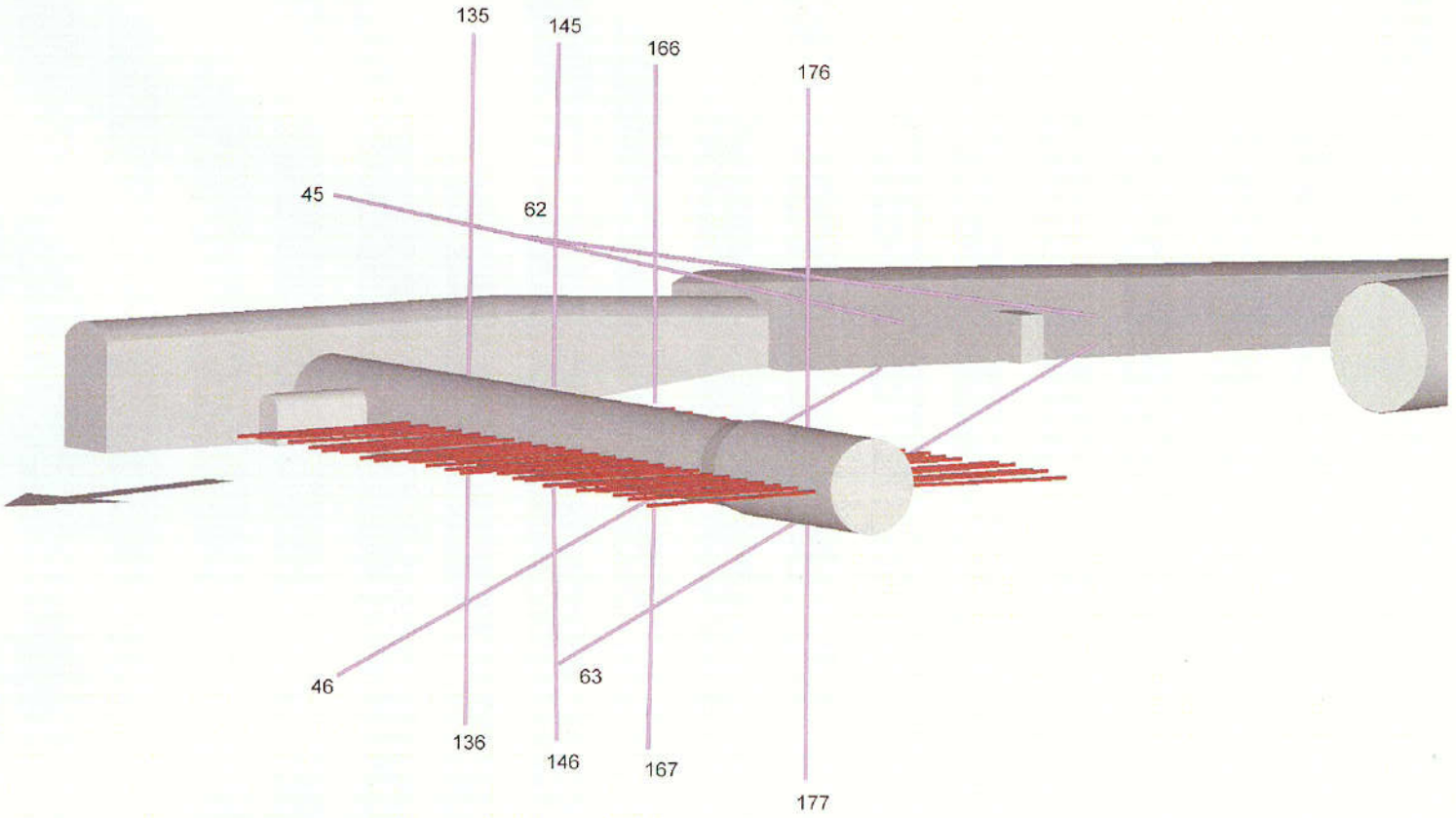

Figure 7. Perspective View Showing ERT Boreholes of the Drift Scale Test.

C30

Table 1. Drift Scale Test Borehole Identification and Locations.

Borehole			Collar			Bottom			Diameter
Number	Identification	Primary Purpose	X (m)	Y (m)	Z (m)	X (m)	Y (m)	Z (m)	(cm)
42	ESF-SDM-42--MPBX-1	MPBX - Rock Mass Displacement	-29.3	13.8	4.6	-3.6	13.7	-0.4	7.7
43	ESF-SDM-43--MPBX-2	MPBX - Rock Mass Displacement	-29.2	21.1	5.1	-3.4	20.7	0.4	7.7
44	ESF-SDM-44--MPBX-3	MPBX - Rock Mass Displacement	-29.5	32.1	5.1	-3.6	32.2	-0.4	7.7
45	ESF-HD-45-ERT-1	Electrical Resistivity Tomography	-28.9	4.6	4.1	9.6	4.7	13.7	7.7
46	ESF-HD-46-ERT-2	Electrical Resistivity Tomography	-27.4	4.6	1.5	9.1	4.5	-14.3	7.7
47	ESF-HD-47-NEU-1	Neutron Probe	-29.1	6.4	4.6	7.2	6.3	21.1	7.7
48	ESF-HD-48-NEU-2	Neutron Probe	-29.1	6.4	4.0	9.5	6.3	13.5	7.7
49	ESF-HD-49-NEU-3	Neutron Probe	-29.0	6.4	3.4	10.8	6.7	7.7	7.7
50	ESF-HD-50-NEU-4	Neutron Probe	-29.0	6.4	2.6	9.7	6.4	-8.1	7.7
51	ESF-HD-51-NEU-5	Neutron Probe	-29.0	6.4	2.3	8.1	6.7	-12.0	7.7
52	ESF-HD-52-CHE-1	Chemistry - SEAMIST	-29.2	8.2	4.5	7.0	8.3	20.1	10.0
53	ESF-HD-53-CHE-2	Chemistry - SEAMIST	-29.2	8.3	4.0	9.4	8.7	13.9	10.0
54	ESF-HD-54-CHE-3	Chemistry - SEAMIST	-29.1	8.2	3.4	10.3	8.4	6.9	10.0
55	ESF-HD-55-CHE-4	Chemistry - SEAMIST	-29.2	8.2	2.6	5.1	8.0	-7.5	10.0
56	ESF-HD-56-CHE-5	Chemistry - SEAMIST	-29.2	8.2	2.3	7.3	8.5	-13.8	10.0
57	ESF-HD-57-HYD-1	Hydrology	-28.8	10.1	4.7	7.8	9.8	19.8	7.7
58	ESF-HD-58-HYD-2	Hydrology	-29.0	10.0	4.1	9.6	10.0	13.7	7.7
59	ESF-HD-59-HYD-3	Hydrology	-29.1	10.0	3.5	10.2	10.0	7.2	7.7
60	ESF-HD-60-HYD-4	Hydrology	-29.1	10.0	2.7	9.2	9.3	-7.3	7.7
61	ESF-HD-61-HYD-5	Hydrology	-29.2	10.1	2.3	8.2	10.2	-12.0	7.7
62	ESF-HD-62-ERT-3	Electrical Resistivity Tomography	-29.2	24.7	6.3	10.1	24.9	13.2	7.7
63	ESF-HD-63-ERT-4	Electrical Resistivity Tomography	-29.3	24.7	4.7	7.0	25.0	-11.9	7.7
64	ESF-HD-64-NEU-6	Neutron Probe	-29.3	26.5	6.6	8.1	26.4	20.8	7.7
65	ESF-HD-65-NEU-7	Neutron Probe	-29.3	26.5	6.3	9.9	26.7	13.7	7.7
66	ESF-HD-66-NEU-8	Neutron Probe	-29.1	26.5	6.0	10.7	26.6	6.9	7.7
67	ESF-HD-67-NEU-9	Neutron Probe	-29.0	26.5	5.2	8.3	25.9	-8.0	7.7
68	ESF-HD-68-NEU-10	Neutron Probe	-29.1	26.6	4.6	6.8	26.9	-12.3	7.7
69	ESF-HD-69-CHE-6	Chemistry - SEAMIST	-29.2	28.4	6.8	8.3	28.7	20.0	7.7

70	ESF-HD-70-CHE-7	Chemistry - SEAMIST	-29.3	28.4	6.3	10.0	29.0	13.1	7.7
71	ESF-HD-71-CHE-8	Chemistry - SEAMIST	-29.4	28.3	6.0	10.7	27.9	6.2	10.0
72	ESF-HD-72-CHE-9	Chemistry - SEAMIST	-29.3	28.4	5.5	8.4	28.8	-8.4	10.0
73	ESF-HD-73-CHE-10	Chemistry - SEAMIST	-29.1	28.4	4.5	6.6	28.5	-12.6	7.7
74	ESF-HD-74-HYD-6	Hydrology	-29.4	30.2	6.8	8.2	30.1	20.6	7.7
75	ESF-HD-75-HYD-7	Hydrology	-29.3	30.2	6.3	10.0	30.5	12.9	7.7
76	ESF-HD-76-HYD-8	Hydrology	-29.3	30.2	6.0	10.7	30.2	6.7	7.7
77	ESF-HD-77-HYD-9	Hydrology	-29.3	30.2	5.7	8.3	29.9	-8.2	7.7
78	ESF-HD-78-HYD-10	Hydrology	-29.4	30.2	4.7	6.5	30.4	-12.9	7.7
79	ESF-HD-79-TEMP-1	Temperature	9.5	-11.0	3.8	9.5	48.5	2.7	10.0
80	ESF-HD-80-TEMP-2	Temperature	-9.5	-11.1	3.2	-9.9	48.6	3.2	10.0
81	ESF-HD-81-MPBX-1	MPBX - Rock Mass Displacement	7.0	-11.1	3.5	6.8	34.9	3.3	7.7
82	ESF-HD-82-MPBX-2	MPBX - Rock Mass Displacement	-7.0	-11.0	3.5	-7.7	35.3	3.1	7.7
83	ESF-HD-83-WH-1	Wing Heater	-2.5	1.8	-0.3	-14.0	1.8	-0.3	10.0
84	ESF-HD-84-WH-2	Wing Heater	-2.5	3.6	-0.2	-14.0	3.7	-0.2	10.0
85	ESF-HD-85-WH-3	Wing Heater	-2.5	5.5	-0.2	-14.1	5.5	-0.3	10.0
86	ESF-HD-86-WH-4	Wing Heater	-2.5	7.3	-0.3	-13.9	7.2	-0.4	10.0
87	ESF-HD-87-WH-5	Wing Heater	-2.6	9.2	-0.3	-14.0	9.3	-0.2	10.0
88	ESF-HD-88-WH-6	Wing Heater	-2.6	11.0	-0.2	-14.0	10.9	-0.2	10.0
89	ESF-HD-89-WH-7	Wing Heater	-2.8	12.8	-0.2	-14.0	12.9	-0.3	10.0
90	ESF-HD-90-WH-8	Wing Heater	-2.5	14.6	-0.3	-14.1	14.5	-0.4	10.0
91	ESF-HD-91-WH-9	Wing Heater	-2.5	16.5	-0.2	-13.8	16.6	-0.2	10.0
92	ESF-HD-92-WH-10	Wing Heater	-2.5	18.3	-0.3	-14.1	18.2	-0.3	10.0
93	ESF-HD-93-WH-11	Wing Heater	-2.4	20.1	-0.3	-14.0	20.1	-0.5	10.0
94	ESF-HD-94-WH-12	Wing Heater	-2.5	22.0	-0.2	-13.9	22.1	-0.2	10.0
95	ESF-HD-95-WH-13	Wing Heater	-2.6	23.8	-0.3	-14.1	23.8	-0.3	10.0
96	ESF-HD-96-WH-14	Wing Heater	-2.6	25.6	-0.3	-14.1	25.7	-0.6	10.0
97	ESF-HD-97-WH-15	Wing Heater	-2.5	27.5	-0.2	-14.1	27.6	-0.4	10.0
98	ESF-HD-98-WH-16	Wing Heater	-2.4	29.2	-0.2	-13.6	29.2	-0.3	10.0
99	ESF-HD-99-WH-17	Wing Heater	-2.6	31.1	-0.3	-14.0	31.3	-0.3	10.0
100	ESF-HD-100-WH-18	Wing Heater	-2.5	32.9	-0.2	-14.0	33.0	-0.3	10.0
101	ESF-HD-101-WH-19	Wing Heater	-2.7	34.7	-0.3	-14.1	34.7	-0.3	10.0

102	ESF-HD-102-WH-20	Wing Heater	-2.6	36.6	-0.3	-14.0	36.4	-0.6	10.0
103	ESF-HD-103-WH-21	Wing Heater	-2.6	38.4	-0.2	-14.2	38.5	-0.2	10.0
104	ESF-HD-104-WH-22	Wing Heater	-2.6	40.2	-0.3	-14.1	40.3	-0.1	10.0
105	ESF-HD-105-WH-23	Wing Heater	-2.6	42.1	-0.3	-14.1	42.2	-0.2	10.0
106	ESF-HD-106-WH-24	Wing Heater	-2.6	43.9	-0.2	-14.1	43.9	-0.2	10.0
107	ESF-HD-107-WH-25	Wing Heater	-2.6	45.7	-0.3	-14.2	45.8	-0.4	10.0
108	ESF-HD-108-WH-26	Wing Heater	2.6	45.7	-0.3	14.1	45.8	-0.5	10.0
109	ESF-HD-109-WH-27	Wing Heater	2.6	43.9	-0.3	14.1	43.8	-0.3	10.0
110	ESF-HD-110-WH-28	Wing Heater	2.6	42.1	-0.3	14.1	42.1	-0.2	10.0
111	ESF-HD-111-WH-29	Wing Heater	2.6	40.2	-0.2	14.1	40.3	-0.1	10.0
112	ESF-HD-112-WH-30	Wing Heater	2.6	38.4	-0.3	14.2	38.3	-0.3	10.0
113	ESF-HD-113-WH-31	Wing Heater	2.6	36.6	-0.2	14.1	36.5	-0.2	10.0
114	ESF-HD-114-WH-32	Wing Heater	2.9	34.8	-0.3	14.3	35.0	-0.3	10.0
115	ESF-HD-115-WH-33	Wing Heater	2.6	32.9	-0.2	14.1	32.7	-0.2	10.0
116	ESF-HD-116-WH-34	Wing Heater	2.7	31.1	-0.3	13.9	31.0	-0.2	10.0
117	ESF-HD-117-WH-35	Wing Heater	2.6	29.2	-0.2	13.8	29.2	-0.1	10.0
118	ESF-HD-118-WH-36	Wing Heater	2.6	27.4	-0.2	14.2	27.4	0.0	10.0
119	ESF-HD-119-WH-37	Wing Heater	2.5	25.6	-0.3	14.1	25.7	-0.4	10.0
120	ESF-HD-120-WH-38	Wing Heater	2.5	23.8	-0.3	14.0	23.8	-0.4	10.0
121	ESF-HD-121-WH-39	Wing Heater	2.5	21.9	-0.3	14.1	21.9	-0.3	10.0
122	ESF-HD-122-WH-40	Wing Heater	2.5	20.1	-0.2	14.1	20.1	-0.2	10.0
123	ESF-HD-123-WH-41	Wing Heater	2.5	18.3	-0.2	14.1	18.3	-0.3	10.0
124	ESF-HD-124-WH-42	Wing Heater	2.5	16.4	-0.3	14.0	16.3	-0.5	10.0
125	ESF-HD-125-WH-43	Wing Heater	2.5	14.6	-0.3	14.0	14.7	-0.5	10.0
126	ESF-HD-126-WH-44	Wing Heater	2.5	12.8	-0.2	14.1	12.9	-0.3	10.0
127	ESF-HD-127-WH-45	Wing Heater	2.6	10.9	-0.3	14.1	10.7	-0.4	10.0
128	ESF-HD-128-WH-46	Wing Heater	2.5	9.1	-0.3	14.0	9.2	-0.4	10.0
129	ESF-HD-129-WH-47	Wing Heater	2.6	7.3	-0.2	14.1	7.1	-0.3	10.0
130	ESF-HD-130-WH-48	Wing Heater	2.6	5.5	-0.2	14.0	5.4	-0.2	10.0
131	ESF-HD-131-WH-49	Wing Heater	2.6	3.7	-0.3	14.1	3.7	-0.3	10.0
132	ESF-HD-132-WH-50	Wing Heater	2.6	1.8	-0.3	14.0	1.6	-0.4	10.0
133	ESF-HD-133-TEMP-3	Temperature	0.7	2.7	2.4	0.9	2.8	22.5	7.7

134	ESF-HD-134-TEMP-4	Temperature	0.7	2.7	-1.6	0.6	2.8	-22.9	7.7
135	ESF-HD-135-ERT-5	Electrical Resistivity Tomography	-0.8	2.7	2.4	-1.0	2.8	22.4	7.7
136	ESF-HD-136-ERT-6	Electrical Resistivity Tomography	-0.8	2.7	-1.6	-0.7	2.6	-18.0	7.7
137	ESF-HD-137-TEMP-5	Temperature	0.8	11.9	2.5	0.9	11.8	22.5	7.7
138	ESF-HD-138-TEMP-6	Temperature	-2.0	11.9	2.0	-16.0	11.5	15.9	7.7
139	ESF-HD-139-TEMP-7	Temperature	-2.6	11.9	0.0	-22.5	12.0	0.1	7.7
140	ESF-HD-140-TEMP-8	Temperature	-1.9	11.9	-1.6	-17.4	11.8	-14.7	7.7
141	ESF-HD-141-TEMP-9	Temperature	0.8	11.9	-1.6	0.6	12.0	-23.0	7.7
142	ESF-HD-142-TEMP-10	Temperature	1.6	11.9	-1.6	16.0	11.9	-15.9	7.7
143	ESF-HD-143-TEMP-11	Temperature	2.7	11.9	0.0	22.5	11.9	0.0	7.7
144	ESF-HD-144-TEMP-12	Temperature	2.0	11.9	2.0	16.4	12.1	16.4	7.7
145	ESF-HD-145-ERT-7	Electrical Resistivity Tomography	-0.8	11.9	2.6	-0.9	12.0	22.7	7.7
146	ESF-HD-146-ERT-8	Electrical Resistivity Tomography	-0.8	11.9	-1.6	-1.1	11.9	-18.0	7.7
147	ESF-HD-147-MPBX-3	MPBX - Rock Mass Displacement	1.3	13.7	2.2	8.7	13.7	15.2	7.7
148	ESF-HD-148-MPBX-4	MPBX - Rock Mass Displacement	-1.4	13.7	2.4	-8.9	13.7	15.2	7.7
149	ESF-HD-149-MPBX-5	MPBX - Rock Mass Displacement	0.0	13.7	2.5	-0.1	13.6	17.6	7.7
150	ESF-HD-150-MPBX-6	MPBX - Rock Mass Displacement	0.0	13.7	-1.6	0.1	13.8	-18.0	7.7
151	ESF-HD-151-REKA-1	Thermal Conductivity and Diffusivity	0.0	17.4	2.7	0.0	17.3	12.7	4.8
152	ESF-HD-152-REKA-2	Thermal Conductivity and Diffusivity	-2.4	17.4	0.0	-12.5	17.2	0.1	4.8
153	ESF-HD-153-REKA-3	Thermal Conductivity and Diffusivity	-1.6	17.4	-1.6	-9.2	17.2	-9.3	4.8
154	ESF-HD-154-MPBX-7	MPBX - Rock Mass Displacement	1.3	21.0	2.2	8.9	21.0	15.1	7.7
155	ESF-HD-155-MPBX-8	MPBX - Rock Mass Displacement	-1.3	21.0	2.3	-9.0	20.9	15.3	7.7
156	ESF-HD-156-MPBX-9	MPBX - Rock Mass Displacement	0.0	21.0	2.5	0.0	20.9	17.5	7.7
157	ESF-HD-157-MPBX-10	MPBX - Rock Mass Displacement	0.0	21.0	-1.6	0.0	21.0	-17.8	7.7
158	ESF-HD-158-TEMP-13	Temperature	0.8	22.8	2.6	0.4	23.0	22.6	7.7
159	ESF-HD-159-TEMP-14	Temperature	-1.9	22.9	1.9	-16.0	22.9	16.2	7.7
160	ESF-HD-160-TEMP-15	Temperature	-2.5	22.9	0.0	-22.6	23.0	0.1	7.7
161	ESF-HD-161-TEMP-16	Temperature	-1.6	22.9	-1.6	-16.0	23.2	-15.9	7.7
162	ESF-HD-162-TEMP-17	Temperature	0.8	22.9	-1.6	0.8	23.0	-22.8	7.7
163	ESF-HD-163-TEMP-18	Temperature	1.5	22.8	-1.6	15.8	22.5	-15.9	7.7
164	ESF-HD-164-TEMP-19	Temperature	2.5	22.9	0.0	22.6	23.0	0.3	7.7
165	ESF-HD-165-TEMP-20	Temperature	1.9	22.8	1.9	16.0	22.8	16.0	7.7

166	ESF-HD-166-ERT-9	Electrical Resistivity Tomography	-0.7	22.8	2.6	-0.6	23.0	22.4	7.7
167	ESF-HD-167-ERT-10	Electrical Resistivity Tomography	-0.8	22.8	-1.6	-0.5	22.7	-17.5	7.7
168	ESF-HD-168-TEMP-21	Temperature	-0.1	32.0	2.5	-0.3	32.0	22.7	7.7
169	ESF-HD-169-TEMP-22	Temperature	0.0	32.0	-1.6	0.3	32.4	-22.9	7.7
170	ESF-HD-170-TEMP-23	Temperature	0.8	39.3	2.5	0.7	39.1	22.6	7.7
171	ESF-HD-171-TEMP-24	Temperature	-1.9	39.3	1.8	-15.6	39.3	15.7	7.7
172	ESF-HD-172-TEMP-25	Temperature	-1.6	39.3	-1.6	-16.0	38.9	-16.0	7.7
173	ESF-HD-173-TEMP-26	Temperature	0.8	39.3	-1.6	0.7	39.1	-22.9	7.7
174	ESF-HD-174-TEMP-27	Temperature	1.6	39.3	-1.6	16.4	38.9	-15.4	7.7
175	ESF-HD-175-TEMP-28	Temperature	1.9	39.3	1.8	15.9	39.2	16.3	7.7
176	ESF-HD-176-ERT-11	Electrical Resistivity Tomography	-0.8	39.3	2.5	-0.8	39.1	22.5	7.7
177	ESF-HD-177-ERT-12	Electrical Resistivity Tomography	-0.7	39.3	-1.6	-0.7	39.3	-17.8	7.7
178	ESF-HD-178-MPBX-11	MPBX - Rock Mass Displacement	1.3	41.1	2.2	8.7	41.1	15.3	7.7
179	ESF-HD-179-MPBX-12	MPBX - Rock Mass Displacement	-1.3	41.1	2.3	-8.8	41.1	15.4	7.7
180	ESF-HD-180-MPBX-13	MPBX - Rock Mass Displacement	0.0	41.1	2.6	0.1	41.1	17.7	7.7
181	ESF-HD-181-MPBX-14	MPBX - Rock Mass Displacement	0.0	41.2	-1.7	0.1	41.2	-18.1	7.7
182	ESF-HD-182-PERM-1	Ambient Characterization	11.6	-15.7	2.3	12.0	-34.5	-4.4	7.7
183	ESF-HD-183-PERM-2	Ambient Characterization	10.7	-15.6	3.0	10.9	-35.7	3.0	7.7
184	ESF-HD-184-PERM-3	Ambient Characterization	8.9	-15.7	2.3	8.9	-34.5	-4.4	7.7
185	ESF-HD-185-HYD-11	Hydrology	-29.5	44.7	7.6	10.1	44.1	13.6	7.7
186	ESF-HD-186-HYD-12	Hydrology	-29.6	44.8	6.5	5.0	44.4	-13.8	7.7
187	ESF-PL-187-MPBX-1	MPBX - Rock Mass Displacement	5.5	-5.1	-0.3	5.5	-8.5	-0.4	7.7
188	ESF-PL-188-MPBX-2	MPBX - Rock Mass Displacement	5.5	-2.8	-0.3	5.5	0.5	-0.3	7.7